A new approach to boundary integral simulations of axisymmetric droplet dynamics

Kazuki Koga

September 25, 2020

Abstract

A novel approach to boundary integral simulations of inviscid droplet dynamics with axial symmetry is proposed. This thesis addresses two computational aspects of the interface problem formulated as axisymmetric vortex sheets with surface tension. The first is a mesh refinement scheme based on signal processing applicable to a variety of moving boundary problems in the plane. A key idea is to directly access the Fourier coefficients of a principal curvature as a function of the arclength through a natural change of variables. The trapezoidal rule is applied to those Fourier-type integrals and the resulting formula fits in the framework of the non-uniform fast Fourier transform. This observation enables to efficiently use an envelope analysis and smoothing filter to generate guidelines for mesh refinement in two singularity formation scenarios. Applications of the concepts also include a non-iterative construction of the uniform parametrization for periodic plane curves, which is utilized in a geometric convergence study of the numerical method involving a rough approximation in the temporal direction. The second is a new regularization technique using singular periodic functions that allows to discretize the axisymmetric Biot-Savart integrals with two promising quadrature rules. In numerical experiments, it is shown that the generalized Gaussian quadrature rules for Müntz systems, which can be found as minimizers to a class of nonlinear least-squares problems, are particularly accurate and fast-converging for the regularized integrands. Combining those with the classical Gauss-Legendre rules, a composite Gaussian quadrature scheme is developed and used to compute a reference solution with high precision for the convergence study in a canonical form.

Acknowledgement

First of all, I would like to thank Professor Toshio Aoyagi, who accepted me as one of his doctoral students at Department of Advanced Mathematical Sciences and encouraged me to acquire invaluable experiences in his research group. Despite the gap between his expertise and the theme of my thesis, he continuously sought opportunities for me to expand my horizons. Especially, learning GPU programming with a brand-new workstation, which he allowed me to customize according to my own purposes, was crucial not only to my success as a doctoral student but to realising how I could improve various aspects of my research skills.

I am also grateful to Professor Jon Wilkening for serving as my mentor during a semester program at ICERM in Providence, where we met in person for the very first time, and hosting my six-month visit to UC Berkeley. Most of the results in this thesis have been polished directly or indirectly by his insightful suggestions and comments, and in particular Chapter 4 is entirely based on our collaborative project initiated at ICERM in 2017. When I applied for the semester program, I was a complete stranger to him and, to be honest, could not imagine that I would have such a wonderful experience in the early stage of my doctoral studies. Moreover, I have been able to freely access his computational environment with a powerful GPU during and after my visit to Berkeley in 2018, which "accelerated" my progress significantly. Without his generosity and patience, I might still be stuck somewhere and struggling to find what I should do.

I am indebted to Professor Takashi Sakajo and Professor Tomoyuki Miyaji at Department of Mathematics in Kyoto University, who have provided me with much advice on my research and offered continuous support since I joined the department as an Office Assistant.

Lastly, I would like to express my highest gratitude to my family for their support and encouragement throughout my graduate studies.

Contents

Chapter 1

Introduction

A deep understanding of droplet motion under the action of surface tension is essential in various engineering applications such as ink-jet printing, spraying, and atomization. There are a large body of literature on theoretical, experimental, and numerical studies of the physics, and significant part of those works is in fact devoted to investigating singularity formations corresponding to self-intersections of a fluid interface from the viewpoint of droplet generation processes. Such phenomena have been of great interest for their universality, richness, and elegant characterizations [1].

To reveal structures of those singularities, numerical simulations play an essential role. However, performing direct simulations based on volumetric equations for the purpose is still too expensive even for a state-of-the-art computer. Hence, it is required to choose a formulation where relevant physical effects can be considered while neglecting factors that do not affect local profiles of singularities. From this point of view, a number of works have focused on boundary integral simulations for potential flow models that describe the motion of an interface separating two inviscid fluids. For example, a two-dimensional droplet formation by a roll-up due to the Kelvin-Helmholtz instability is carefully studied by Hou et al. [2] (henceforth HLS97). In an axisymmetric case, Leppinen and Lister [3] investigates the self-similarity of inviscid capillary pinch-off for a range of density jumps across the surface of a droplet. Their results are more firmly confirmed by Nitsche and Steen [4] (henceforth NS04) with additional insights into the nature of the self-similarity. Furthermore, a recent work by Burton and Taborek [5] revisits pinch-off of two-dimensional droplets and finds that the type of the singularity is distinctly different from that of its axisymmetric counterpart.

Besides the dimension of the problem being reduced by one, a main advantage of boundary integral simulations is its flexibility in controlling computational mesh. The successful works mentioned above undoubtedly rest on mesh refinement schemes that dynamically redistribute computational points densely in the regions of interest. However, the strategies employed in the previous studies are highly problem-specific. That is, it is required to know "a priori" a few important properties of given initial conditions, which precludes applications of those methods to general cases. For instance, the method by NS04, which is presumably the most sophisticated one among those tailored techniques, starts from the uniform mesh and advects discrete points in a continuous manner toward a prescribed distribution that reflects the symmetry of their initial conditions. In singular interface problems, a major barrier to a design of more automatic mesh refinement schemes is that a pointwise quantity such as curvatures shows very complicated behavior near a singularity, and is therefore unable to define an effective mesh distribution on the fly, even though the regions of interest are often visually evident from the graph of that function.

To address this problem, this thesis proposes a novel mesh refinement strategy with tools from signal processing for resolving singularity formations in the vortex sheet formulation of axisymmetric droplet dynamics driven by surface tension. A vortex sheet is a sharp interface separating two inviscid, incompressible, and irrotational fluids shearing past each other, which has a boundary integral formulation that derives from the Biot-Savart law [6]. Identifying the surface of an axisymmetric droplet with a periodic plane curve, guidelines for our mesh refinement scheme, which replace the prescribed distribution in NS04, are generated based on an envelope analysis and smoothing filter applied to the curvature in the symmetry plane as a function of the arclength (or equivalently, its Fourier coefficients). Such a combination extracts an outline of the complexity of an evolving curve from its sharp curvature profile, and provides practical information on a desirable mesh distribution in a much simpler form. It turns out that the procedure is capable of detecting singularity formations with far less human intervention than the existing methods, provided that highly complex geometry does not appear in a very short time. On the other hand, the Fourier coefficients with the arclength variable are discretized by the trapezoidal rule after a natural change of variables, and the resulting discrete formula is approximated with $\mathcal{O}(N \log N)$ complexity by the non-uniform fast Fourier transform [7], an emerging algorithm in computational harmonic analysis. In practice, we

test the numerical scheme on the pair of initial conditions studied by Nie [8] (henceforth Nie01) that reach two distinct types of singularities at the end, and discuss several aspects of our strategy related to its efficiency, accuracy, and limitations.

A philosophy behind the signal processing approach is that an evolving plane curve should carry some information invariant under a change of parametrization, which is the "geometric" Fourier coefficients of the curvature in the present work. This is a simple, but very useful paraphrase of the principle shared by the community; the shape of a moving boundary is completely determined by its normal velocity, as rigorously proved by Epstein and Gage [9] for the mean curvature flow in the plane. In fact, applications of the Fourier coefficients with the arclength variable include a non-iterative algorithm for constructing the uniform parametrization of periodic plane curves, which implies that a parametric curve retains its canonical representation in the background. Such an idea enables comparisons between two discretized curves with different mesh distributions, and is fully utilized in revealing the convergence of the time-stepping procedure of NS04, which is essential for implementing our mesh refinement scheme in a straightforward manner at the cost of controlling several important parameters during simulations.

As part of the validation, we develop a new regularization technique for the axisymmetric Biot-Savart integrals in the case of spherical geometry. With the periodic representation of the axisymmetric surface, non-integrable factors in the integrands are regarded as periodic functions and directly regularized using singular functions defined on the unit circle. This strategy allows to apply two fast-converging quadrature rules to the regularized integrands, the generalized Gaussian rules for Müntz systems [10] and the Double-Exponential rule [11]. In this thesis, those Gaussian quadrature rules are formulated as solutions to a class of nonlinear least-squares problems and computed iteratively by the Levenberg–Marquardt algorithm. Our numerical experiments show that both methods converge superalgebraically and the generalized Gaussian rules outperform the other. Using these results, a composite Gaussian quadrature scheme is suggested and used to compute a reference solution with high precision in the convergence study of our numerical method.

The rest of this thesis is organized as follows. Chapter 2 introduces a boundary integral formulation of axisymmetric vortex sheets with surface tension and two relevant initial conditions. Chapter 3 describes the theory behind our mesh refinement strategy based on signal processing. Chapter 4

develops new approximation schemes for the axisymmetric Biot-Savart integrals and investigates their performances. Chapter 5 explains our practical numerical method and some technicalities in its implementation. Chapter 6 presents numerical results and validates the implemented scheme. Concluding remarks are given in Chapter 7.

This thesis is primarily based on one accepted paper by the author [12], and Chapter 4 is based on one paper in preparation by the author and Wilkening [13].

Chapter 2

Formulations

In this chapter, we give a brief introduction to boundary integral equations for axisymmetric vortex sheets with surface tension, which is followed by a short description of finite-time singularities in the formulation reported by other authors. For interested readers, a more detailed derivation can be found in NS04.

2.1 Lagrangian Theory

We consider irrotational motion of two inviscid, incompressible, and immiscible fluids in $\mathbb{R}^3$ separated by a closed surface S. In the following, the inner and outer fluid are denoted by Ω_1 and Ω_2, respectively, and Ω_1 is assumed to be simply-connected. For simplicity, we also assume that the density of each fluid is uniformly equal to unity and that no external force acts on the system. Then, the fluid velocity $\mathbf{u}_i$ and pressure p_i in Ω_i $(i = 1, 2)$ satisfy the Euler equations, the equation of continuity, and the rotation-free condition

$$\frac{\partial \mathbf{u}_i}{\partial t} + (\mathbf{u}_i \cdot \nabla)\mathbf{u}_i = -\nabla p_i, \quad \nabla \cdot \mathbf{u}_i = 0, \quad \nabla \times \mathbf{u}_i = 0, \tag{2.1}$$

with the boundary conditions

$$\mathbf{u}_i(\mathbf{x}, t) \to 0 \quad \text{as} \quad \|\mathbf{x}\| \to \infty \quad \text{(far-field condition)}, \tag{2.2}$$

$$[\mathbf{u}]_S \cdot \mathbf{n} = 0 \quad \text{on } S \quad \text{(kinematic boundary condition)}, \tag{2.3}$$

$$[p]_S = \sigma\kappa \quad \text{on } S \quad \text{(Laplace-Young condition)}, \tag{2.4}$$

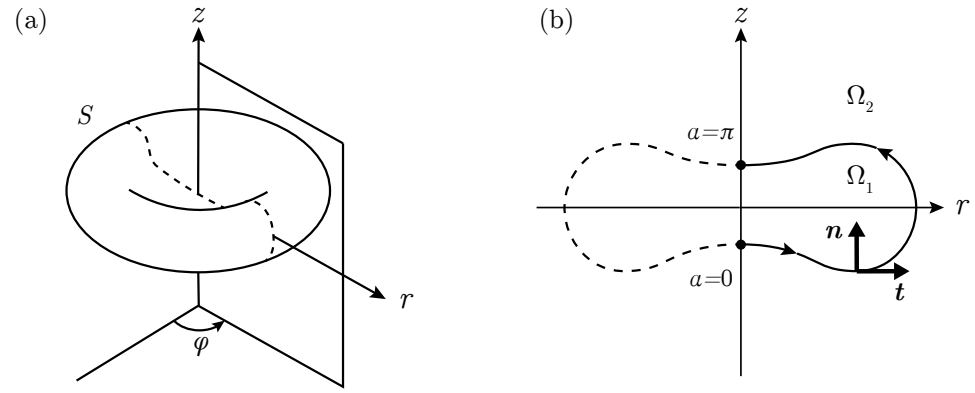

Figure 2.1: Sketch illustrating: (a) axial symmetry, (b) parametrization in r–z plane.

where $\mathbf{x}$ and t are the spatial and time variable, respectively. Also, $\mathbf{n}$ is the unit normal vector of S pointing to Ω_1, κ is twice the mean curvature that is positive if S is a sphere, and σ is a positive surface tension coefficient. The brackets $[\cdot]_S$ measure the jump of a function across S as follows:

$$[f]_S(\mathbf{x},t) = \lim_{\substack{\mathbf{y}\to\mathbf{x}\\ \mathbf{y}\in\Omega_1}} f_1(\mathbf{y},t) - \lim_{\substack{\mathbf{y}\to\mathbf{x}\\ \mathbf{y}\in\Omega_2}} f_2(\mathbf{y},t), \quad \mathbf{x}\in S. \tag{2.5}$$

The far-field condition (2.2) states that the fluid at infinity is at rest. The kinematic boundary condition (2.3) requires that the normal component of the fluid velocity must be continuous across S, while the tangential component can be discontinuous there. The Laplace-Young condition (2.4) represents the effects of surface tension on S in terms of the mean curvature and the pressure jump across the interface.

Throughout the rest of this thesis, we assume that the flow is axially symmetric. That is, in some cylindrical coordinates (r,φ,z), all functions describing the flow are independent of the azimuthal coordinate φ (see Fig. 2.1(a)). In this setting, for tracking the motion of a free surface S, it suffices to solve time evolution of the intersection of S and a symmetry plane $\varphi = \text{const}$. Thus, we parametrize the curve in the r–z plane by

$$\mathbf{X}(\alpha,t) = (r(\alpha,t), z(\alpha,t)), \quad \alpha\in[0,\pi], \tag{2.6}$$

where r and z are radial and axial coordinates, respectively, and find its

evolution equation in the form

$$\frac{\partial \mathbf{X}}{\partial t} = U\mathbf{n} + V\mathbf{t}. \tag{2.7}$$

Again, $\mathbf{n}$ is the unit normal vector pointing to Ω_1, and $\mathbf{t}$ is the unit tangent vector in the counterclockwise direction. In particular, we set $r(0,t) = r(\pi,t) = 0$ for all t, and direct $\mathbf{X}$ so that it satisfies $\mathbf{t} = \mathbf{X}_\alpha/s_\alpha$ (see Fig. 2.1(b)). Here, the subscript α denotes differentiation with respect to the variable α, and $s_\alpha = \sqrt{r_\alpha^2 + z_\alpha^2}$ is called the *relative spacing* that is the derivative of the arclength s measured from the starting point $\mathbf{X}(0,t)$. In the present case, the kinematic boundary condition (2.3) implies that $U = \mathbf{W}\cdot\mathbf{n}$, where $\mathbf{W}$ is the average of the fluid velocities on either side of S, whereas it puts no restriction on V. In fact, it is well-known that the shape of an evolving plane curve is determined solely by the normal velocity U, and the tangential velocity V only affects the relative spacing s_α.

To obtain an integral form of $\mathbf{W}$, we introduce a dynamical variable γ called the *unnormalized vortex sheet strength* that measures the jump of the tangential component of the fluid velocity in a frame-dependent manner:

$$\gamma(\alpha,t) = \mathbf{X}_\alpha \cdot [\mathbf{u}]_S(\mathbf{X}(\alpha,t),t), \quad \alpha \in [0,\pi]. \tag{2.8}$$

Then, assuming that the azimuthal component of the fluid velocity is uniformly zero (i.e. without swirl), the Biot-Savart law and the Plemelj's formula imply that $\mathbf{W} = (w_r, w_z)$ is given by the Cauchy's principal values (denoted by dashed integrals)

$$w_r(\alpha,t) = \frac{1}{2\pi}\fint_0^\pi \left(\frac{\gamma'}{\rho_2}\right)\left(\frac{\xi}{r}\right)\left[K(\lambda) - \frac{\xi^2 + r^2 + r'^2}{\rho_1^2}E(\lambda)\right]d\alpha', \tag{2.9}$$

$$w_z(\alpha,t) = \frac{1}{2\pi}\fint_0^\pi \left(\frac{\gamma'}{\rho_2}\right)\left[K(\lambda) - \frac{\xi^2 + r^2 - r'^2}{\rho_1^2}E(\lambda)\right]d\alpha', \tag{2.10}$$

where $\xi = z' - z$ and, for example, $r = r(\alpha,t)$ and $r' = r(\alpha',t)$ (e.g., see [14] for details). Here, K and E are the complete elliptic integrals of the first and second kind, respectively. Other functions in (2.9) and (2.10) are defined as

$$\rho_1^2 = \xi^2 + (r'-r)^2, \quad \rho_2^2 = \xi^2 + (r'+r)^2, \quad \lambda^2 = 4rr'/\rho_2^2. \tag{2.11}$$

On the other hand, the evolution equation for γ is a consequence of the unsteady Bernoulli's theorem and the Laplace-Young condition (2.4):

$$\frac{\partial \gamma}{\partial t} = -\sigma\kappa_\alpha + ((V - \mathbf{W}\cdot\mathbf{t})\gamma/s_\alpha)_\alpha. \tag{2.12}$$

In axisymmetric geometry, it is convenient to express κ as the sum of

$$\kappa_z = \frac{z_{\alpha\alpha} r_\alpha - z_\alpha r_{\alpha\alpha}}{s_\alpha^3}, \quad \kappa_r = \frac{z_\alpha}{s_\alpha r}, \tag{2.13}$$

which are the principal curvatures in the symmetry plane and in a plane normal to it, respectively. Without surface tension (i.e. $\sigma = 0$), the first term in the right-hand side of (2.12) is absent, and choosing $V = \mathbf{W} \cdot \mathbf{t}$ renders γ time-independent. This special choice for V is often referred to as the *Lagrangian frame*, and it has been studied mainly in the context of the famous Moore's singularity [15]. With surface tension, however, it is no longer straightforward to keep γ conserved in time. Moreover, it is known that the Lagrangian frame typically leads to rapid decreases in s_α at points where geometry is not necessarily complex, as demonstrated by HLS97 and NS04. These facts motivate us to choose V to control the relative spacing s_α for other practical purposes.

Following Hou et al. [16] (henceforth HLS94), we switch from the Cartesian coordinates to the so-called angle–arclength variables (θ, s_α) that satisfy

$$\mathbf{X}_\alpha = (s_\alpha \cos\theta, s_\alpha \sin\theta). \tag{2.14}$$

Having these new dynamical variables, we are able to reconstruct (r, z) up to a translation by integrating Eq. (2.14). Such a loss of information is not a problem here, for the current interest lies in developing mesh refinement schemes to resolve singularity formations due to self-intersections of the interface S. The evolution equations for (θ, s_α) follow from the orthogonal decomposition in (2.7), the Frenet-Serret formula for plane curves, and the identity $\theta_\alpha = s_\alpha \kappa_z$:

$$\frac{\partial \theta}{\partial t} = \frac{U_\alpha + V\theta_\alpha}{s_\alpha}, \tag{2.15}$$

$$\frac{\partial s_\alpha}{\partial t} = V_\alpha - \theta_\alpha U. \tag{2.16}$$

Eq. (2.16) is central to the present work. As mentioned earlier, because of the tangential velocity being arbitrary, the relative spacing s_α can be controlled by a user-specified V while keeping the image of $\mathbf{X}$ unchanged. In fact, this can be done by deriving a desirable s_α first and calculating V accordingly based on Eq. (2.16). Our choice for V is described in detail in Chapter 3.

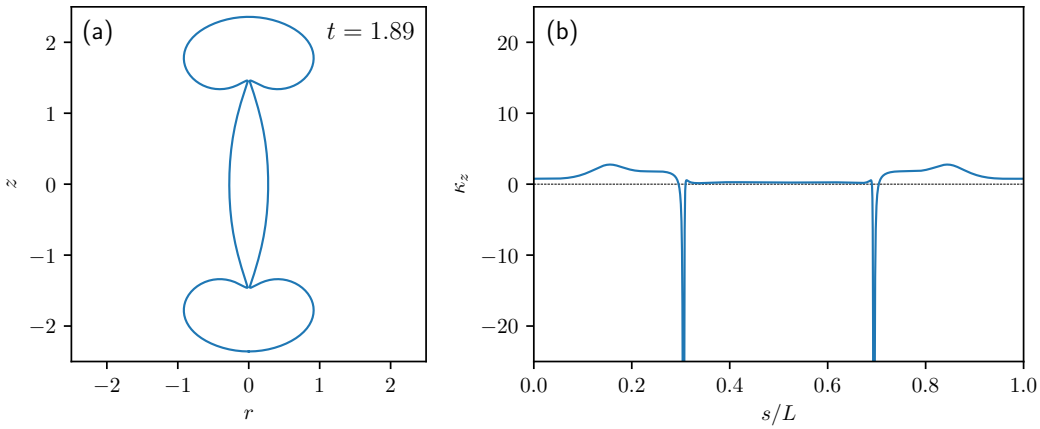

Figure 2.2: Solution close to singularity for pinch-off problem (2.17): (a) interface position in r–z plane, (b) profile of curvature κ_z.

2.2 Singularity Formations

It is well-known that, without any regularization, the dynamics of vortex sheets is subject to the Kelvin-Helmholtz instability and generally leads to the Moore's singularity [15]. On the other hand, HLS94 points out that surface tension acts as a dispersive regularization of the Kelvin-Helmholtz instability, and also reports that numerical solutions with $\sigma \neq 0$ continue beyond the Moore's singularity for the initial condition studied by Krasny [17] in the zero surface tension setting. Instead of the Moore's singularity, however, several works have found that other kinds of singularities appear when a fluid interface self-intersects. Such phenomena are often called *topological singularities*.

The most famous topological singularity is presumably *capillary pinch-off*, which is characterized by a fast drop in the radius of a neck due to surface tension acting on the azimuthal curvature κ_r. To study this process numerically with the vortex sheet formulation, Nie01 proposes the initial condition

$$\sigma = 0.2, \quad \theta(\alpha, 0) = \alpha, \quad s_\alpha(\alpha, 0) = 1, \quad \gamma(\alpha, 0) = -2\sin(2\alpha). \tag{2.17}$$

Qualitatively, this problem resembles an experiment by Robinson and Steen [18]. As an intuitive illustration, we show in Fig. 2.2 a snapshot of a numerical solution starting from (2.17) and the corresponding curvature κ_z as a function

of s divided by the total arclength $L = s(\pi, t)$. As seen in Fig. 2.2(a), the solution is symmetric with respect to the r–axis and eventually forms two end-droplets at the top and bottom along with an elongated satellite droplet in between. Also, one can easily see that overturning occurs in each pinch-off region, which precludes descriptions of the process by a single-valued function of z. NS04 studies the same problem numerically to confirm the self-similarity of inviscid capillary pinch-off

$$r_{\min} \sim (t_p - t)^{\frac{2}{3}}, \quad (z_{\min} - z_p) \sim (t_p - t)^{\frac{2}{3}}, \tag{2.18}$$

for a range of density jumps across the interface. Here, $(r_{\min}, z_{\min})$ are the coordinates of a point that attains the minimum neck radius, z_p is the axial coordinate where the pinch-off occurs, and t_p is the time when the radius $r_{\min}$ reaches exactly zero. From a numerical simulation perspective, the initial condition (2.17) is particularly suitable for an accurate numerical study on the scaling law (2.18), for it has an additional line symmetry and the shape of the interface is considerably simple away from the necks (see Fig. 2.2(b)). In the present work, this problem is revisited to assess efficiency and accuracy of our numerical schemes.

Another scenario of topological singularity formations is self-intersections due to inertia resisted by surface tension. In the present formulation, this singularity is found for the initial condition

$$\sigma = 0.04, \quad \theta(\alpha, 0) = \alpha, \quad s_\alpha(\alpha, 0) = 1, \quad \gamma(\alpha, 0) = -\sin(\alpha), \tag{2.19}$$

which is also suggested by Nie01. This situation can be understood as a uniform flow past a sphere [19] where the solid boundary is instantly dissolved at $t = 0$ and evolves under the action of surface tension. Again, Fig. 2.3 plots a numerical solution starting from (2.19) and its curvature κ_z. As seen in Fig. 2.3(a), the interface collides itself away from the axis of symmetry, and the droplet seems to break into a torus-like component and a simply-connected one. For brevity, we refer to this type of singularities as *bag breakup*. The nature of bag breakup is expected to be different from that of capillary pinch-off, because in this case surface tension should always tend to restore the droplet to a spherical shape. Regarding this point, motivated by their own experiments [20], Burton and Taborek [5] numerically investigates bag breakup in two-dimensional flows (called *2D pinch-off* by the same authors), and they find that its self-similarity is of the second kind. That is, the local behavior of a fluid interface close to a self-intersection is characterized by the memory of an initial condition, and the spatial variables follow

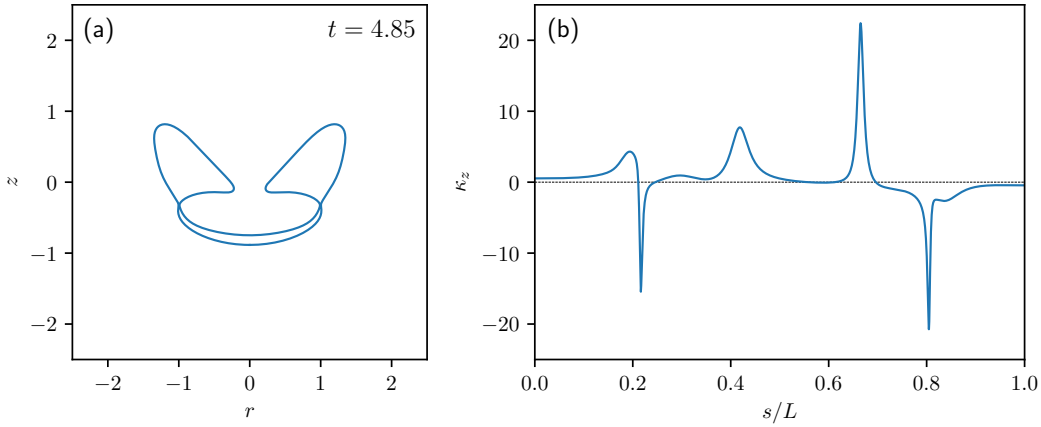

Figure 2.3: Solution close to singularity for axisymmetric bag breakup (2.19): (a) interface position in r–z plane, (b) profile of curvature κ_z.

scaling laws with different exponents. Furthermore, by using the full model and its "slender" approximation, they find numerical evidences of those self-similarity exponents distinct from that of (2.18). We speculate that a similar analysis may be applicable to the axisymmetric case. In this thesis, however, we do not aim to identify the similarity exponents in the axisymmetric bag breakup (2.19), because it forms multiple high-curvature regions away from the self-intersection and is therefore inappropriate for that purpose (see Fig. 2.3(b)). Rather, our interest lies in whether it is possible to develop a mesh refinement scheme that is able to capture singularity formations and such high-curvature regions simultaneously.

Chapter 3

Mesh Refinement

3.1 Basic Theory

The choice of the tangential velocity V, which we have left undefined so far, is crucial in numerical simulations of evolving plane curves. This is particularly true if one needs to resolve small-scale structures of a fluid interface approaching an imminent singularity formation. In the context of potential flow models, several works use the Lagrangian frame $V = \mathbf{W} \cdot \mathbf{t}$ in a combination with some remeshing techniques. For example, in simulations of capillary pinch-off with axial symmetry, Leppinen and Lister [3] advects computational points by the Lagrangian frame and redistributes them at each time step in order to keep the relative spacing proportional to the distance from the point of the minimum neck radius. A similar strategy is used by Burton and Taborek [5] to study bag breakup in two-dimensional flows. Although this idea provides a simple way of accumulating points to high-curvature regions, it does not naturally extend to general cases because their methods heavily rely on the fact that the initial conditions studied in those works lead to self-intersections right on a targeted coordinate axis.

In the following, we employ a style in mesh refinement that harnesses the arbitrariness of the tangential velocity V. Namely, the equation for V that realizes a given s_α is derived for a simple open curve identified with an axisymmetric surface whose inner region is simply connected, which implies

$$V(0,t) = V(\pi,t) = 0, \tag{3.1}$$

for all t. At a glance, this condition might seem to limit the applicability of our method. However, with minor modifications to (3.1), we believe that

our ideas easily extend to the cases of periodic plane curves in general and unbounded curves with periodic boundary conditions.

Following HLS94, we define the relative spacing s_α as the total arclength L multiplied by a positive function R whose integral over $[0, \pi]$ is equal to 1:

$$s_\alpha(\alpha, t) = R(\alpha, t)L(t), \quad \int_0^\pi R d\alpha = 1. \tag{3.2}$$

By differentiating both sides of the first equation in (3.2) with respect to t and substituting the result into (2.16), we get

$$V_\alpha = \left(\frac{\partial R}{\partial t} L + R \frac{dL}{dt} \right) + \theta_\alpha U. \tag{3.3}$$

Also, by combining (2.16) and (3.1), it is easy to see that

$$\frac{dL}{dt} = -\int_0^\pi \theta_\alpha U d\alpha. \tag{3.4}$$

Now, by integrating (3.3) with (3.1), we obtain the following equation for V:

$$V(\alpha, t) = \int_0^\alpha \left(\frac{\partial R'}{\partial t} L + R' \frac{dL}{dt} \right) d\alpha' + \int_0^\alpha \theta'_\alpha U' d\alpha'. \tag{3.5}$$

The uniform parametrization, by which we mean that s_α is independent of the variable α, corresponds to $R \equiv \pi^{-1}$ [16]. In this case, Eq. (3.5) is explicitly solved for V as

$$V(\alpha, t) = -\frac{\alpha}{\pi} \int_0^\pi \theta_\alpha U d\alpha + \int_0^\alpha \theta'_\alpha U' d\alpha'. \tag{3.6}$$

The uniform parametrization is a typical choice for various moving boundary problems because, unlike the Lagrangian frame, it prevents computational points from clustering at undesired locations and maintains stable spatial discretization. However, it is almost obvious that this is not the best option for accurate numerical studies of singularity formations in general. From this point of view, for a two-dimensional droplet formation by a Kelvin-Helmholtz roll-up, HLS97 alternatively proposes a variable but time-independent R with a few minima, which is empirically constructed from numerical results for the same problem with the uniform parametrization. A major advantage of this method is that it is still possible to solve Eq. (3.5) explicitly for V in the

same form as (3.6), but such a function R is literally problem-specific by definition.

As an extension of HLS97, NS04 suggests a strategy for constructing a variable and time-dependent R to solve the pinch-off problem (2.17). Their choice for R is initially uniform and develops exactly two symmetric minima at $\alpha = \alpha_c$ and $\alpha = \pi - \alpha_c$. More specifically, they first prescribe the function

$$g(x) = 1.125 + \delta(\cos(4x) - \cos(2x)), \quad \delta = \delta_{\max}\frac{t}{t_p}, \tag{3.7}$$

for some constant $\delta_{\max}$, and compose it with a monotonically increasing function $q(s)$ that also evolves in time and allows the two minima of $g(q)$ to dynamically follow the points of the minimal neck radius. Using this composite function $g(q)$, they define the function R as

$$R(\alpha, t) = \frac{g(q(s(\alpha)))}{\int_0^\pi g(q(s(\alpha')))d\alpha'}, \tag{3.8}$$

and apply it to the initial condition (2.17) for a range of density jumps across the interface. Although their computations are successful in many aspects, it has to be said that this definition is still specialized to a class of initial conditions with a line symmetry. Moreover, it requires to know in advance the pinch-off time t_p, the number of singular points, and even a characterization of the point $(r_{\min}, z_{\min})$ that never causes $q(s)$ to be discontinuous in time.

The main difficulty in the design of mesh refinement for singular interfacial problems is that the curvature κ_z, a pointwise measure of the complexity of a plane curve, is by itself unlikely to define a promising candidate for R. Intuitively, there are two reasons for this consideration. Firstly, as shown in Fig. 2.2(b), a peak in κ_z that corresponds to a self-intersection can be significantly sharp and therefore, if R is written in terms of κ_z, the relative spacing s_α may reflect this sharpness as a dynamical variable. Secondly, it is found in Fig. 2.3(b) that there is an inflection point (i.e. a point where the sign of κ_z changes) in a small interval where the gradient of κ_z is very steep, which causes s_α to increase locally and magnifies $\kappa_{z,\alpha}$ many times. A similar situation can be seen in Fig. 2.2(b), and it is numerically verified in NS04 that there exists at least one inflection point in the self-similar regime (2.18). In fact, to our knowledge, no previous study succeeds in resolving self-intersections of a fluid interface with mesh refinement based on pointwise evaluations of κ_z. Nevertheless, there is no doubt that the graphs of

the curvature κ_z visually show where singularities are about or at least likely to appear. In some sense, the previous works draw rough sketches of such visual cues as their function R with the help of numerical experiments or theoretical considerations.

3.2 Signal Processing Approach

We attempt to further extend the idea of NS04 by developing a new tool that automatically generates guideline functions, denoted by GL, in place of the composite function $g(q)$. In particular, we automate the "sketching" process by applying an envelope analysis and smoothing filter from signal processing to the curvature κ_z as a periodic function of the arclength s. For this purpose, the first step is to extend the parametric curve $\mathbf{X}$ to the interval $[0, 2\pi]$ with the symmetry

$$r(\pi + \alpha, t) = -r(\pi - \alpha, t), \quad z(\pi + \alpha, t) = z(\pi - \alpha, t), \tag{3.9}$$

as illustrated in Fig. 2.1(b), and consider the Fourier coefficients

$$\hat{f}(k) = \frac{1}{L_p} \int_0^{L_p} f(s) e^{-2\pi i k \frac{s}{L_p}} ds, \tag{3.10}$$

where L_p denotes the total arclength of the periodic curve $\mathbf{X}$. These quantities can be accessed via the natural change of variables $ds = s_\alpha d\alpha$:

$$\frac{1}{L_p} \int_0^{L_p} f(s) e^{-2\pi i k \frac{s}{L_p}} ds = \frac{1}{L_p} \int_0^{2\pi} (f(s(\alpha)) s_\alpha) e^{-2\pi i k \frac{s(\alpha)}{L_p}} d\alpha, \tag{3.11}$$

and are expected to be invariant under a change of parametrization that preserves the starting point $\mathbf{X}(0, t)$ and the direction of increasing α. This property is essential as an element of mesh refinement, because we cannot construct an appropriate R from any frame-dependent information.

Next, we introduce the so-called *analytic signal* [21]

$$A[f](s) = f(s) + i\mathcal{H}[f](s), \tag{3.12}$$

where $\mathcal{H}$ is the Hilbert transform, which is the Fourier multiplier of the form

$$\widehat{\mathcal{H}[f]}(k) = (-i\mathrm{sgn}(k)) \cdot \hat{f}(k). \tag{3.13}$$

Hence, the Fourier coefficients of $A[f]$ vanish for all negative wavenumbers, and the term "analytic" derives from the fact that such a periodic function, if it is considered on the unit circle, can be extended to a holomorphic function on the unit disk. In classical harmonic analysis, the operator A plays important roles in the study of the convergence of the Fourier series for p-integrable functions with $1 < p < \infty$ [22]. On the other hand, in signal processing, the analytic signal is often called a *pre-envelope*, because, by rewriting $A[f]$ as

$$A[f](s) = E[f](s)e^{i\psi(s)}, \tag{3.14}$$

one can extract the *analytic envelope* [23]

$$E[f](s) = \sqrt{f(s)^2 + (\mathcal{H}[f](s))^2}. \tag{3.15}$$

Here, the angle ψ is called the instantaneous phase, which is also defined in terms of f and its Hilbert transform. Roughly speaking, the analytic envelope is expected to have a low frequency content in comparison to that of the complex exponential factor in (3.14). We explain this property with the simplest example presented by Cohen [24]. Suppose that we have a smooth complex-valued function $A(x) = E(x)e^{ik_0 x}$ with a 2π-periodic real-valued E and an integer $k_0 > 0$. Then, the Fourier coefficients of A are those of E shifted to the right by k_0, and, for A to be "analytic", the coefficients of E must be zero for wavenumbers $k < -k_0$. By the conjugate symmetry for real-valued functions, this means that all the non-zero Fourier coefficients of E are contained within the range $-k_0 \leq k \leq k_0$, and the strict inequalities hold if the function A is zero-mean. Unfortunately, it is very hard to show the same property for periodic functions in general. Instead, to illustrate some tendencies, the analytic envelope is demonstrated in Fig. 3.1 for the following functions:

$$G_p(x) = e^{-64(x-C_1)^2}\sin(\omega(x - C_1)) + e^{-64(x-C_2)^2}\cos(\omega(x - C_2)), \tag{3.16}$$
$$G_s(x) = \sin(x)\sin(8x), \tag{3.17}$$

where $C_1 = \frac{\pi}{2}$, $C_2 = \frac{3}{2}\pi$, and $\omega = 16$. The signal G_p is a superposition of two Gaussian pulses [25] that have compact numerical supports because of the fast decaying prefactors. We show the raw G_p and its analytic envelope in Fig. 3.1(a). Here, note that the left pulse has one zero point between two peaks with different signs, while the right pulse has one sharp peak surrounded by multiple zero points. In both cases, the operator E ignores

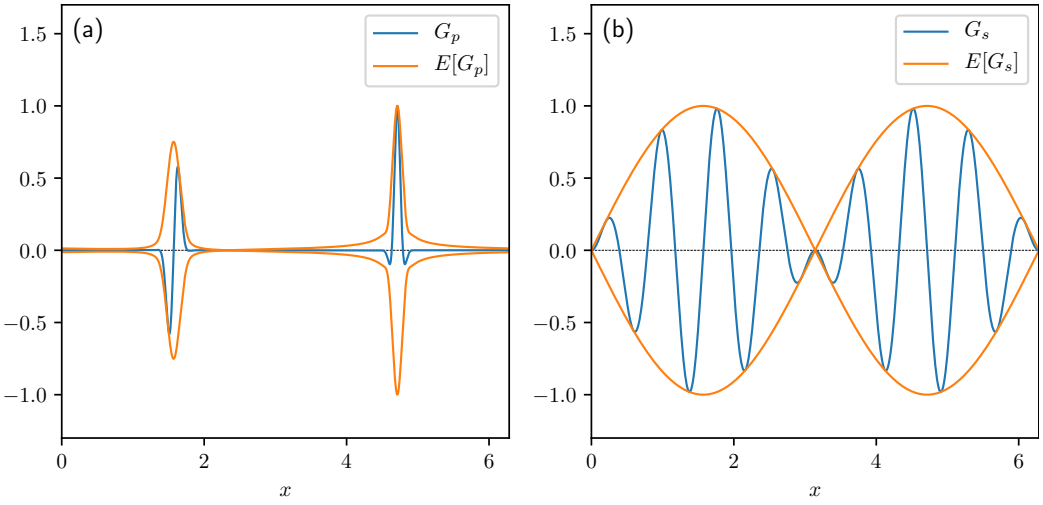

Figure 3.1: Signals and corresponding analytic envelopes: (a) Gaussian pulses G_p, (b) product of two sine functions G_s.

all these zero points and transforms the original pulses to simple and strictly positive peaks. Therefore, it is anticipated that the analytic envelope can remove the difficulty caused by inflection points near self-intersections. On the other hand, the signal G_s is a product of sine functions with a high and low frequency, as shown in Fig. 3.1(b). In this case, the operator E fails to detect any local complexity, presumably due to the low-frequency nature of the analytic envelope, and simply returns a function similar to $|\sin x|$. These results imply that the analytic envelope is effective only if high-curvature regions are localized and sufficiently isolated from each other. Moreover, the second example shows that the analytic envelope can be non-differentiable at zero points of the original signal. To avoid this problem, we replace (3.15) with a regularized envelope

$$E_r[f](s) = \sqrt{1 + (E[f](s))^2}. \tag{3.18}$$

Adding a constant inside the square root renders the final form of GL slightly less sharp, but this regularization is clearly inevitable for the sake of smoothness. Also, it should be noted that the analytic envelope of a nearly-singular function is inherently very sharp. In this thesis, to obtain GL smoother than the original κ_z, we apply the Gaussian filter to the analytic envelope $E_r[\kappa_z]$.

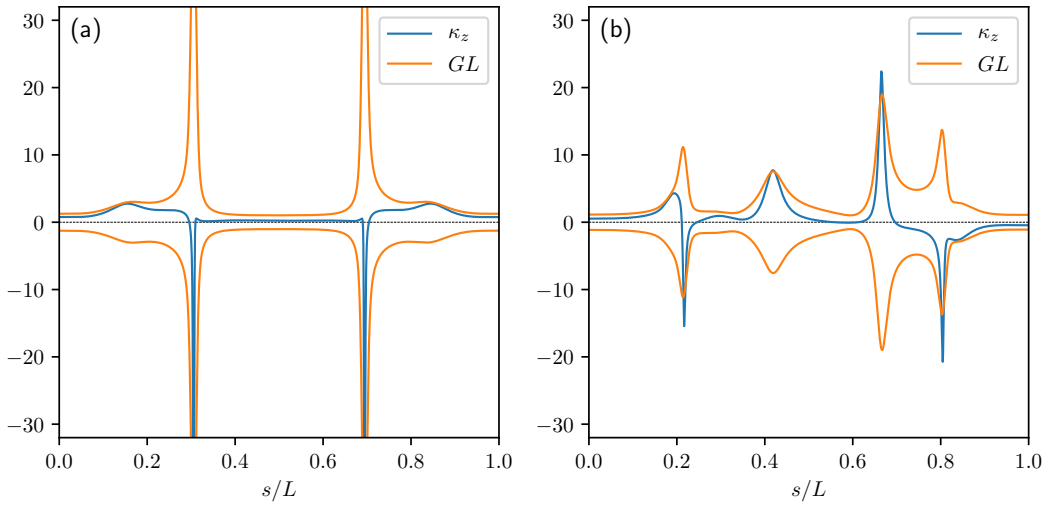

Figure 3.2: Curvature κ_z and generated guideline function GL at times close to singularity: (a) pinch-off problem at $t = 1.89$, (b) axisymmetric bag breakup at $t = 4.85$.

That is, the function $E_r[\kappa_z]$ is convolved with the heat kernel

$$H_a(s) = (a^2/\pi)^{\frac{1}{2}} e^{-a^2 s^2}, \tag{3.19}$$

where the parameter a controls the level of smoothing and essentially determines the locality of mesh refinement. To summarize, we suggest the following guideline function GL as a "rough" measure of the complexity of an evolving plane curve:

$$GL(s) = (E_r[\kappa_z] * H_a)(s) \tag{3.20}$$

In Fig. 3.2, the functions GL with $a = 20$ are shown for the curvature κ_z in Fig. 2.2(b) and Fig. 2.3(b). In both cases, our technique is successful in generating simple and strictly positive functions that outline relevant features of the original signals κ_z.

Finally, we define the relative spacing s_α in terms of the guideline function GL. In our definition, the function R is split into a few components using a parameter δ_R, which determines the maximal amount of refinement, and another Gaussian as a function of the time t:

$$R(\alpha, t) = (1 - \delta_R)\{(1 - e^{-dt^2})R_e + e^{-dt^2} R_0\} + \delta_R R_0, \quad d > 0. \tag{3.21}$$

Here, R_0 and R_e are defined as

$$R_0(\alpha, t) = \frac{1}{\pi}, \quad R_e(\alpha, t) = \frac{GL(s(\alpha), t)^{-1}}{\int_0^\pi GL(s(\alpha'), t)^{-1} d\alpha'}, \tag{3.22}$$

and these definitions trivially guarantee that

$$\int_0^\pi R_0 d\alpha = \int_0^\pi R_e d\alpha = \int_0^\pi R d\alpha = 1. \tag{3.23}$$

Moreover, it is easy to show that the definition (3.21) satisfies the relations

$$R(\alpha, 0) = R_0, \quad \frac{\partial R}{\partial t}(\alpha, 0) = 0. \tag{3.24}$$

Hence, at $t = 0$, the parametrization is uniform and the tangential velocity V is given by the formula (3.6). At $t \neq 0$, however, the equation (3.5) is no longer solvable explicitly for V. To circumvent this problem, NS04 suggests the backward difference approximation

$$\frac{\partial R}{\partial t}(\alpha, t) \approx \frac{R(\alpha, t) - R(\alpha, t - \tau)}{\tau}, \tag{3.25}$$

for some $\tau > 0$. This formula allows to find V in the same way as for the time-independent R, although errors of $\mathcal{O}(\tau)$ are introduced to the relative spacing s_α. We suggest a convenient choice of τ in Chapter 5, and a validation of Eq. (3.25) is given in Chapter 6.

Chapter 4

Special Quadrature Rules

In this chapter, we develop special approximation schemes for the axisymmetric Biot-Savart integrals based on a new regularization technique and fast-converging quadrature rules for the so-called Müntz systems. One of those schemes is used in Chapter 6 to compute a reference solution in the convergence study of a numerical method involving the finite difference (3.25).

4.1 Existing Methods

Let B_r and B_z denote the integrands in (2.9) and (2.10), respectively. These subscripts are also used for functions associated with those integrands, but are omitted if relations hold for both cases. Following Nitsche [26], the polynomial expansions of $K(\lambda)$ and $E(\lambda)$ for $\lambda \approx 1$ [27]

$$K(\lambda) \approx \log 4 + \sum_{n=1} a_{K,n}\zeta^n - \left(\frac{1}{2} + \sum_{n=1} b_{K,n}\zeta^n\right)\log\zeta, \tag{4.1}$$

$$E(\lambda) \approx 1 + \sum_{n=1} a_{E,n}\zeta^n - \left(\sum_{n=1} b_{E,n}\zeta^n\right)\log\zeta, \tag{4.2}$$

where $\zeta = 1 - \lambda^2$, followed by the Taylor expansions at $\alpha' = \alpha$ reveal

$$B(\alpha,\alpha',t) = B^*(\alpha,\alpha',t) + \frac{c_{-1}(\alpha,t)}{\alpha'-\alpha} + \sum_{n=0}^{\infty} c_n(\alpha,t)(\alpha'-\alpha)^n \log|\alpha'-\alpha|. \tag{4.3}$$

Here, B^* is the smooth part of B and, in general, $c_{-1} \neq 0$ and $c_n \neq 0$ for infinitely many n, which precludes the additive construction of a function that represents all the singularities in (4.3). Furthermore, another difficulty in the case of spherical geometry is that the derivatives of B and the coefficients c_n show some singular behavior near the axis of symmetry. More precisely, Nitshce [26] proves that when $\alpha \approx 0$

$$\frac{\partial^k B_r}{\partial \alpha'^k}(\alpha, 0, t) \sim \frac{1}{\alpha^{k-1}}, \quad c_{n,r}(\alpha, t) \sim \frac{1}{\alpha^{n-1}}, \tag{4.4}$$

for B_r, and similarly

$$\frac{\partial^k B_z}{\partial \alpha'^k}(\alpha, 0, t) \sim \frac{1}{\alpha^{k}}, \quad c_{n,z}(\alpha, t) \sim \frac{1}{\alpha^{n}}, \tag{4.5}$$

for B_z, and the same asymptotics hold for $\alpha' = \pi$ and $\alpha \approx \pi$. Thus, applying a simple quadrature rule to the integrals (2.9) and (2.10) can lead to highly non-uniform discretization errors, as found by de Bernardinis and Moore [28].

There have been two major directions for addressing this problem. Firstly, Nie and Baker [29] switch to finding a potential and a pseudo-steamfunction formulated as boundary integrals whose integrands are bounded and continuous. Their method splits the well-behaved integrands into smooth and singular parts using the expansions (4.1) and (4.2), and then applies the adaptive Gauss-Kronrod quadrature rule [30] to the former and the modified Clenshaw-Curtis quadrature rule [31] to the latter. With appropriate interpolants, each algorithm adaptively inserts nodes near the axis of symmetry and improves approximations to a prescribed relative tolerance. A drawback of their strategy is, however, that the velocity (w_r, w_z) is found via formulae involving the first and second derivatives of the potential and pseudo-streamfunction, and some additional errors are inevitably introduced through numerical differentiation. Another successful work is the class of approximation schemes developed by Nitsche [26] based on the Euler-Maclaurin formula for the trapezoidal rule, which extends the naive third-order method by de Bernardinis and Moore [28]. In their strategy, following error analysis by Sidi and Israeli [32], high-order corrections are computed in terms of the derivatives of B and the coefficients c_n that can be found with the help of symbolic calculation softwares such as Mathematica. To obtain uniform discretization errors, they also construct approximate integrands that model the singular behavior of B near the axis of symmetry to a given finite order.

A major advantage of their method is that the approximate integrands have some self-similar properties and integrals of those functions can be precomputed up to some time-dependent prefactors. Moreover, such an idea can be applicable beyond the axisymmetric vortex sheet problems [33]. However, the convergence of a scheme based on the Euler-Maclaurin formula is algebraic by definition, and it requires to write down explicitly the derivatives of B and the coefficients c_n.

4.2 Regularization with Periodic Extensions

We aim to develop direct approximation schemes for the axisymmetric Biot-Savart integrals (2.9) and (2.10) with superalgebraic convergences. In this direction, it is desirable to first remove the non-integrable term in the right-hand side of (4.3), because quadrature rules with such efficiency are typically intended for integrable functions. However, integrating a singular function with high precision often requires its values at points sufficiently close to the singularity. Thus, a clever regularization technique is also needed for accurate evaluations of integrands at nearly arbitrary points.

To see resemblances between B_r and B_z, we introduce the new notations

$$F = \frac{\gamma'}{2\pi\rho_2}, \quad P_r = \left(\frac{\xi}{\rho_1^2}\right)\{\xi^2 + r^2 + r'^2\}, \quad P_z = \frac{\xi^2 + r^2 - r'^2}{\rho_1^2}, \tag{4.6}$$

and rewrite the integrands as

$$B_r = r^{-1}F[\xi K(\lambda) - P_r E(\lambda)], \quad B_z = F[K(\lambda) - P_z E(\lambda)]. \tag{4.7}$$

In both cases, the terms involving $K(\lambda)$ are at most logarithmically singular and hence integrable, although it is not straightforward to evaluate $K(\lambda)$ for $\alpha' \approx \alpha$. On the other hand, the factor P introduces the leading-order term in (4.3) due to the denominator ρ_1^2 vanishing at $\alpha' = \alpha$, while the elliptic integral $E(\lambda)$ is bounded and even continuous.

A main idea in our strategy is to regularize P without expanding the whole B. For this purpose, considering r and z as periodic functions on $[0, 2\pi]$, we note that the function P can also be extended to a singular periodic function on $[0, 2\pi]$. Then, if there exists a periodic function J that has a singularity of the same kind as P, the difference $P - cJ$ for some constant c is a smooth periodic function that can be sampled on equispaced grids containing $\alpha' = \alpha$, which enables to evaluate $P - cJ$ at arbitrary points

via its truncated Fourier series. In the present work, the choice for J is

$$J(\alpha,\alpha') = \frac{1}{\cos\alpha}\frac{\sin\alpha' - \sin\alpha}{(\cos\alpha'-\cos\alpha)^2 + (\sin\alpha'-\sin\alpha)^2} \tag{4.8}$$

for $\alpha \in [0, \frac{\pi}{4}] \cup [\frac{3\pi}{4}, \pi]$, and

$$J(\alpha,\alpha') = -\frac{1}{\sin\alpha}\frac{\cos\alpha' - \cos\alpha}{(\cos\alpha'-\cos\alpha)^2 + (\sin\alpha'-\sin\alpha)^2} \tag{4.9}$$

for $\alpha \in [\frac{\pi}{4}, \frac{3\pi}{4}]$. Note that this definition requires to switch between the two different J because neither of them is numerically stable for every $\alpha \in [0,\pi]$.

Now, we apply our regularization technique to B_r:

$$\begin{aligned}
\fint_0^\pi B_r d\alpha' &= \frac{1}{r}\fint_0^\pi F[\xi K(\lambda) - P_r E(\lambda)]d\alpha' \\
&= \frac{1}{r}\int_0^\pi F[\xi K(\lambda) - (P_r - c_{P,r}J)E(\lambda)]d\alpha' \\
&\quad - \frac{c_{P,r}}{r}\fint_0^\pi FJE(\lambda)d\alpha' \\
&= \frac{1}{r}\int_0^\pi F[\xi K(\lambda) - (P_r - c_{P,r}J)E(\lambda)]d\alpha' \\
&\quad - \frac{c_{P,r}}{r}\int_0^\pi F\left(J - \frac{1}{\alpha'-\alpha}\right)E(\lambda)d\alpha' \\
&\quad - \frac{c_{P,r}}{r}\fint_0^\pi \left(\frac{1}{\alpha'-\alpha}\right)FE(\lambda)d\alpha'.
\end{aligned} \tag{4.10}$$

Here, c_P is the coefficient of the leading-order term of P near $\alpha' = \alpha$, while the corresponding value of J is normalized. For the detail of the asymptotics of P and J, see (A.1)–(A.3) in Appendix A. Similarly for B_z, we have

$$\begin{aligned}
\fint_0^\pi B_z d\alpha' &= \fint_0^\pi F[K(\lambda) - P_z E(\lambda)]d\alpha' \\
&= \int_0^\pi F[K(\lambda) - (P_z - c_{P,z}J)E(\lambda)]d\alpha' \\
&\quad - c_{P,z}\int_0^\pi F\left(J - \frac{1}{\alpha'-\alpha}\right)E(\lambda)d\alpha' \\
&\quad - c_{P,z}\fint_0^\pi \left(\frac{1}{\alpha'-\alpha}\right)FE(\lambda)d\alpha'.
\end{aligned} \tag{4.11}$$

Again, the factor $P - c_P J$ is a smooth periodic function that can be well approximated by its truncated Fourier series. On the other hand, $[J-(\alpha'-\alpha)^{-1}]$ is a smooth function whose values at arbitrary points can be precomputed using multiple-precision floating-point arithmetics. Finally, the non-integrable factor of the shared integral in Eqs. (4.10)(4.11) is eliminated by integrating by parts:

$$\begin{aligned}
\fint_0^\pi \left(\frac{1}{\alpha'-\alpha}\right) FE(\lambda)d\alpha' &= \lim_{\epsilon\to 0}\left(\int_0^{\alpha-\epsilon} \frac{1}{\alpha'-\alpha} FE(\lambda)d\alpha' \right.\\
&\qquad \left. + \int_{\alpha+\epsilon}^{\pi} \frac{1}{\alpha'-\alpha} FE(\lambda)d\alpha'\right)\\
&= \lim_{\epsilon\to 0}\left(\left[\log|\alpha'-\alpha| FE(\lambda)\right]_0^{\alpha-\epsilon}\right.\\
&\qquad \left. + \left[\log|\alpha'-\alpha| FE(\lambda)\right]_{\alpha+\epsilon}^{\pi}\right)\\
&\quad - \int_0^\pi \log|\alpha'-\alpha| \frac{\partial}{\partial\alpha'}(FE(\lambda))d\alpha'\\
&= -\int_0^\pi \log|\alpha'-\alpha| \frac{\partial}{\partial\alpha'}(FE(\lambda))d\alpha'. \qquad (4.12)
\end{aligned}$$

In the above calculation, the end-point values vanish due to the continuity of $FE(\lambda)$ and the fact that the vortex sheet strength γ must be zero on the z-axis in order for the axial symmetry to be preserved. Also, to evaluate the integral (4.12), we utilize the formula

$$\frac{dE}{d\lambda}(\lambda) = \frac{E(\lambda)-K(\lambda)}{\lambda}, \qquad (4.13)$$

which relates the derivative of E to K and E itself.

In summary, the axisymmetric Biot-Savart integrals (2.9) and (2.10) can be recasted via the following relations:

$$\fint_0^\pi B_r d\alpha' = \frac{1}{r}\int_0^\pi F[\xi K(\lambda) - (P_r - c_{P,r}J)E(\lambda)]d\alpha' - \frac{c_{P,r}}{r}\int_0^\pi Q d\alpha', \quad (4.14)$$

$$\fint_0^\pi B_z d\alpha' = \int_0^\pi F[K(\lambda) - (P_z - c_{P,z}J)E(\lambda)]d\alpha' - c_{P,z}\int_0^\pi Q d\alpha', \quad (4.15)$$

where the universal integrand Q is given as

$$\begin{aligned} Q = F\left(J - \frac{1}{\alpha' - \alpha}\right) E(\lambda) \\ - \log|\alpha' - \alpha| \left[\frac{\partial F}{\partial \alpha'} E(\lambda) + \left(\frac{1}{\lambda}\frac{\partial \lambda}{\partial \alpha'} F\right)(E(\lambda) - K(\lambda))\right]. \end{aligned} \tag{4.16}$$

Before moving on to quadrature rules, two important aspects of the new function Q should be mentioned. Firstly, since it has the term involving both $K(\lambda)$ and $\log|\alpha' - \alpha|$, one may expect the leading-order term of Q to be $\log^2|\alpha' - \alpha|$. Fortunately, however, it can be easily shown that another factor $\partial\lambda/\partial\alpha'$ always vanishes at $\alpha' = \alpha$. Thus, using the same procedure as for the expansion (4.3), we have

$$\begin{aligned} Q(\alpha, \alpha', t) = Q^*(\alpha, \alpha', t) \\ + \sum_{n=0}^{\infty} c_{n,Q}(\alpha, t)(\alpha' - \alpha)^n \log|\alpha' - \alpha| \\ + \sum_{n=1}^{\infty} d_{n,Q}(\alpha, t)(\alpha' - \alpha)^n \log^2|\alpha' - \alpha|, \end{aligned} \tag{4.17}$$

and the only unbounded term in (4.17) is $\log|\alpha' - \alpha|$. Secondly, the factor $\lambda^{-1}(\partial\lambda/\partial\alpha')$ contains r'^{-1} that is unbounded at $\alpha' = 0$, π, while F contains γ' that smoothly vanishes at the same points. Therefore, it is crucial to group those factors as $\lambda^{-1}(\partial\lambda/\partial\alpha')F$, so that the reciprocal γ'/r' can be factored out and evaluated via its truncated Fourier series. This observation allows to avoid a potential source of large round-off errors near the axis of symmetry.

4.3 Applications of Quadrature Rules

There are at least two kinds of fast-converging quadrature rules for functions with singularities of the type (4.17). The first is the *generalized Gaussian quadrature rules* for Müntz systems, which are linearly-independent collections of finitely many functions in the form $x^k \log^l x$, typically with pairs of non-negative integers (k, l). Since such a family of functions constitutes a Chebyshev system [34], there exists a unique m-point quadrature rule that integrates exactly each member of a Müntz system with $2m$ functions [35]. However, in contrast to the Gauss-Legendre theory [36], a characterization

of the exact rules for Müntz systems is non-trivial, and it is often necessary to find their nodes and weights with the help of some numerical optimization techniques [10]. The second is the *Double-Exponential (DE) quadrature rule* [11], which transplants an integrand into the whole real-line using a transformation whose derivative decays so fast that the truncated trapezoidal rule effectively becomes exponentially convergent. As opposed to the generalized Gaussian rules, it is straightforward to find nodes and weights of the DE rule, and it seems promising in view of the behavior (4.4) and (4.5), because a broad class of singularities can be handled at both end-points with just the single formula. However, a great drawback of the DE rule is that it is very delicate in floating-point arithmetics and can suffer from underflow, overflow, and cancellation errors, as demonstrated by Trefethen and Weideman [37] with a simple example. Moreover, another problem with typical DE transformations is their poor resolution property, which is shown by Adcock et al. [38] in the context of polynomial approximations of functions with end-point singularities. Roughly speaking, they show that $\mathcal{O}(\omega \log(\omega))$ sample points are needed for a modified Fourier basis to resolve the complex exponential $e^{i\omega x}$ trasplanted by a classical DE transformation, whereas the original function on $[0, 2\pi]$ requires only $\mathcal{O}(\omega)$ points for the Fourier and Chebyshev basis.

Generalized Gaussian Quadrature Rules

Here, we formulate generalized Gaussian quadrature rules as minimizers to a class of nonlinear least-squares problems. For Müntz systems, those optimization problems are efficiently solved by the Levenberg–Marquardt method [39] after the Gram-Schmidt process for square-integrable functions. This is a special case of the situations considered in [13], where a broader class of functions are handled with some practical strategies for reducing the number of iterations. In a similar direction, Bremer et al. [40] develops an optimization scheme based on the damped Gauss–Newton method [41], which replaces the numerically unstable continuation scheme by Ma et al. [10] for Chebyshev systems with additional requirements. Given $2m$ square-integrable functions, which do not necessarily constitute a Chebyshev system, their algorithm starts by finding a discretization of the collection based on a piecewise Legendre quadrature rule that preserves all the L^2 inner products. After performing an orthonormalization in the discrete representation, a $2m$–point Chebyshev quadrature rule for the conditioned basis is constructed as an

initial guess of a nonlinear least-squares problem with quadrature nodes and weights as its unknowns. Then, the algorithm repeatedly attempts to reduce the size of the quadrature rule by choosing one node to remove at each iteration and applying the damped Gauss–Newton method to the smaller problem until it obtains a m-point Gaussian or a nearly Gaussian quadrature rule. In contrast, the following approach begins with a m-point quadrature rule, because the existence of a unique m-point Gaussian rule is guaranteed for a Müntz system of $2m$ functions. Furthermore, the number of unknowns in our method is m rather than $2m$, for we seek not a whole quadrature rule but a set of quadrature nodes.

Given a Müntz system $\{\varphi_i\}_{1\leq i\leq 2m}$ on the interval $(0,1)$, we find a m–point quadrature rule $\{(x_i, w_i)\}_{1\leq i\leq m}$ that satisfies

$$\sum_{j=1}^{m} w_j \varphi_i(x_j) = \int_0^1 \varphi_i(x)dx, \quad (i = 1, \ldots, 2m). \tag{4.18}$$

In Eq. (4.18), the exact integral of a function in the form $x^k \log^l x$ is

$$\int_0^1 x^k \log^l x dx = \frac{(-1)^l l!}{(k+1)^{l+1}}. \tag{4.19}$$

Hence, a Müntz system is not (even nearly) orthonormal with respect to the L^2 inner product. When given such a poorly conditioned basis, our algorithm does not necessarily return the desired m–point quadrature rule. To avoid this consequence, the system $\{\varphi_i\}$ is orthonormalized by the Gram-Schmidt process with the explicit formula (4.19), and the Gaussian quadrature rule is sought for the resulting collection $\{u_i\}$. For this purpose, it is required to represent the orthonormal basis $\{u_i\}$ as linear combinations of the original $\{\varphi_i\}$ (see Appendix B). However, there is no way to perform the procedure for a highly ill-conditioned system without using multi-precision floating-point arithmetics, because the coefficients of such representations can be extremely large and cause severe cancellations. In our code, both the Gram-Schmidt process and evaluations of the orthonormal basis are performed in floating-point arithmetics with precision that depends on the size of a given Müntz system. On the other hand, all the numerical linear algebras involved in the following optimization process are performed in the standard double-precision or long double-precision arithmetics, and the minimal use of extended precisions cannot be too expensive.

For any $\mathbf{x} = (x_1, \ldots, x_m)^\mathsf{T}$ such that $0 < x_1 < \cdots < x_m < 1$, we define the $2m \times m$ matrix $\mathbf{A}(\mathbf{x}) = (A_{ij}(\mathbf{x}))$ and the vector $\mathbf{b} = (b_1, \ldots, b_{2m})^\mathsf{T}$ via

$$A_{ij}(\mathbf{x}) = u_i(x_j), \quad b_i = \int_0^1 u_i(x)dx. \tag{4.20}$$

Then, the desired Gaussian quadrature rule with the nodes $\mathbf{x}$ and the corresponding weight $\mathbf{w} = (w_1, \ldots, w_m)^\mathsf{T}$ should satisfy the linear equations

$$\mathbf{A}(\mathbf{x})\mathbf{w} = \mathbf{b}. \tag{4.21}$$

Now, let $\mathbf{A} = \mathbf{U}\mathbf{S}\mathbf{V}^\mathsf{T}$ be the singular value decomposition, and define $\mathbf{w}$ to be the least-squares solution $\mathbf{w} = \mathbf{V}\mathbf{S}^{-1}\mathbf{U}^\mathsf{T}\mathbf{b}$ as a vector-valued function of $\mathbf{x}$. Obviously, an initial guess of $\mathbf{x}$ is unlikely to coincide with the correct answer and should have a non-zero residual

$$\mathbf{r}(\mathbf{x}) = (r_1, \ldots, r_{2m})^\mathsf{T} = \mathbf{b} - \mathbf{A}\mathbf{w}. \tag{4.22}$$

Conversely, if the residual $\mathbf{r}(\mathbf{x})$ is zero, the uniqueness of the exact quadrature rule implies that the vector $\mathbf{w}$ consists of the quadrature weights compatible with the nodes $\mathbf{x}$. Thus, computing the generalized Gaussian quadrature rule for a Müntz system is reduced to the minimization problem of an appropriate norm of the residual $\mathbf{r}(\mathbf{x})$ with the unknown $\mathbf{x}$. Since the max norm is not easy to optimize and differs by at most a factor of $\sqrt{2m}$ from the two norm, we instead minimize

$$f(\mathbf{x}) = \frac{1}{2}\mathbf{r}(\mathbf{x})^\mathsf{T}\mathbf{r}(\mathbf{x}). \tag{4.23}$$

In summary, we find the generalized Gaussian quadrature rule for a Müntz system by numerically solving the following nonlinear least-squares problem:

$$\min_{\mathbf{x}} \|f(\mathbf{x})\|, \quad f(\mathbf{x}) = \frac{1}{2}\mathbf{r}(\mathbf{x})^\mathsf{T}\mathbf{r}(\mathbf{x}), \tag{4.24}$$

with the residual $\mathbf{r}$ given in (4.22) and the unknown vector $\mathbf{x} = (x_1, \ldots, x_m)^\mathsf{T}$ satisfying $0 < x_1 < \cdots < x_m < 1$. The minimization problem (4.24) can be efficiently solved by the Levenberg-Marquardt method with a diagonal scaling. The Jacobi matrix of $\mathbf{r}$ is also expressed in terms of the elements of the decomposition $\mathbf{A} = \mathbf{U}\mathbf{S}\mathbf{V}^\mathsf{T}$ [13]:

$$\mathbf{J} = \left(\frac{\partial r_i}{\partial x_j}\right) = -\mathbf{U}\mathbf{S}^{-1}\mathbf{V}^\mathsf{T}\mathrm{diag}(\mathbf{B}^\mathsf{T}\mathbf{r}) - (\mathbf{I} - \mathbf{U}\mathbf{U}^\mathsf{T})\mathbf{B}\mathrm{diag}(\mathbf{w}), \tag{4.25}$$

where $\mathbf{B} = (B_{ij}(\mathbf{x})) = (\frac{du_i}{dx}(x_j))$ and diag($\mathbf{v}$) is the diagonal matrix with a vector $\mathbf{v}$ as diagonal elements. In a nonlinear least-squares problem, the Jacobi matrix (4.25) often provides sufficient information for the oprimization process. That is, for a function in the form (4.23), the gradient $\mathbf{g}$ and an approximation of the Hessian $\mathbf{H}$ are computed in terms of $\mathbf{J}$ and $\mathbf{r}$:

$$\mathbf{g} = \nabla f = \mathbf{J}^\mathsf{T}\mathbf{r}, \quad \mathbf{H} = \left(\frac{\partial^2 f}{\partial x_i \partial x_j}\right) \approx \mathbf{J}^\mathsf{T}\mathbf{J}. \tag{4.26}$$

As a trust-region algorithm, the Levenberg-Marquardt method seeks at each iteration the minimizer of the quadratic function

$$f^*(\mathbf{p}) = f(\mathbf{x}) + \mathbf{g}^\mathsf{T}\mathbf{p} + \frac{1}{2}\mathbf{p}^\mathsf{T}\tilde{\mathbf{H}}\mathbf{p}, \quad \tilde{\mathbf{H}} = \mathbf{J}^\mathsf{T}\mathbf{J}, \tag{4.27}$$

in the vicinity of the current state $\mathbf{x}$. To preserve the strictly increasing order of $\mathbf{x}$, the diagonal matrix

$$\mathbf{D} = (D_{ij}), \quad D_{jj} = 2/\min(x_j - x_{j-1}, x_{j+1} - x_j), \tag{4.28}$$

is introduced, and the minimizer $\mathbf{p}^*$ of the function (4.27) is sought inside the elllpse $\|\mathbf{D}\mathbf{p}\|_2 \leq \Delta$. Here, the trust-region radius $\Delta \leq 1$ is updated at each iteration by estimating the quality of the model function (4.27) with the criterions given in [39]. With a diagonal scaling, it is well known that the minimizer $\mathbf{p}^*$ is found by solving the linear least-squares problem

$$\min_{\mathbf{p}} \left\| \begin{pmatrix} \mathbf{J} \\ \Lambda\mathbf{D} \end{pmatrix} \mathbf{p} + \begin{pmatrix} \mathbf{r} \\ 0 \end{pmatrix} \right\|, \tag{4.29}$$

In the linear sub-problem (4.29), the scalar Λ, often called the damping factor, is set to be positive if $\mathbf{p}^*$ violates the condition $\|\mathbf{D}\mathbf{p}^*\|_2 \leq \Delta$ for $\Lambda = 0$. Since the two norm of the vector $\mathbf{D}\mathbf{p}^*$ can be written down in terms of the singular values of $\mathbf{J}$, an appropriate parameter Λ is found by the Newton's method so that the vector $\mathbf{p}^*$ satisfies $\|\mathbf{D}\mathbf{p}^*\|_2 \approx \Delta$ [39]. On the other hand, the solution $\mathbf{p}^*$ for $\Lambda = 0$ that satisfies $\|\mathbf{D}\mathbf{p}^*\|_2 \leq \Delta$ is equivalent to the step of the Gauss-Newton method, which shows quadratic convergences in the final stages of the algorithm.

In our stable implementation, the linear least-squares problem (4.29) is solved using the singular value decomposition, and the entire Levenberg-Marquardt method continues until it achieves $f(\mathbf{x}) < 10^{-30}$. As a test problem, our algorithm is first applied to the system

$$\{1, ..., x^{24}, \log x, .., x^{24}\log x\}, \tag{4.30}$$

whose Gaussian quadrature rule is tabulated in [10]. With Chebyshev nodes in $(0,1)$ as an initial guess of $\mathbf{x}$, the algorithm takes 240 iterations to converge in the double-precision floating-point arithmetics, while 498 iterations are needed for evenly spaced nodes in $(0,1)$. In most cases, including the Müntz systems below, Chebyshev nodes are somewhat superior to uniform nodes as initial inputs, presumably because the former resolves more densely the small interval near the end-point $x = 0$. Next, we attempt to compute the generalized Gaussian quadrature rules for Müntz systems of the form

$$\{1, ..., x^{k^*-1}, \log x, .., x^{k^*-1}\log x, x\log^2 x, ..., x^{k^*-1}\log^2 x\}. \tag{4.31}$$

These collections contain terms in the expansion (4.17) whose polynomial factors are at most of order k^*-1. As mentioned earlier, the term $\log^2 x$ is not included here, because in Eqs. (4.14)(4.15) the leading-order term of the most singular integrand Q is $\log|\alpha' - \alpha|$. For the systems (4.31), our algorithm is capable of generating the Gaussian quadrature rules up to $k^* = 65$ (i.e. a 97-point rule) in the long double-precision arithmetics. Unfortunately, finding Gaussian rules for even larger k^* is not feasible for the current code, mainly due to its computational costs. In our numerical experiments, however, it turns out that even such a small quadrature rule is sufficient for achieving satisfactory approximations of a typical example.

Double-Exponential Quadrature Rule

For the Double-Exponential quadrature rule, we choose the tanh-sinh transformation suggested by Takahasi and Mori [11]:

$$\phi_{\mathrm{DE}}(x) = \tanh\left(\frac{\pi}{2}\sinh(x)\right), \quad \frac{d\phi_{\mathrm{DE}}}{dx}(x) = \frac{\frac{\pi}{2}\cosh(x)}{\cosh^2(\frac{\pi}{2}\sinh(x))}. \tag{4.32}$$

The change of variables with ϕ_{DE} transplants a function on $[-1,1]$ to one on the whole real-line, and moves the end-point singularities to $x = \pm\infty$:

$$\int_{-1}^{1} f(y)dy = \int_{-\infty}^{\infty} f(\phi_{\mathrm{DE}}(x))\frac{d\phi_{\mathrm{DE}}}{dx}(x)dx. \tag{4.33}$$

Then, the integral on the right-hand side of (4.33) is discretized by the truncated trapezoidal rule as

$$\int_{-\infty}^{\infty} f(\phi_{\mathrm{DE}}(x))\frac{d\phi_{\mathrm{DE}}}{dx}(x)dx \approx \Delta x \sum_{k=-m}^{m} f(\phi_{\mathrm{DE}}(k\Delta x))\frac{d\phi_{\mathrm{DE}}}{dx}(k\Delta x). \tag{4.34}$$

In fact, a precise rate of convergence of the formula (4.34) is determined by the analyticity of f and the decay rates of $f(\phi_{\mathrm{DE}})$ as $|x| \to \infty$. However, because of the double-exponential behavior $\frac{d\phi_{\mathrm{DE}}}{dx}(x) = \mathcal{O}(\exp(-\frac{1}{4}\pi e^{|x|}))$, this quadrature rule shows superlinear convergences for a wide class of functions with end-point singularities, including each logarithmic term in the expansion (4.17). In theory, the optimal rate of convergence can be achieved by finding the size m and the spacing Δx that balance the discretization error and the truncation error. As discussed in [37], the former error is estimated by $\mathcal{O}(\exp(-2\pi a/\Delta x))$ for some $a \leq \frac{\pi}{2}$, while the latter is $\mathcal{O}(\exp(-\frac{\pi}{2}e^{m\Delta x}))$. By equating these two, we obtain

$$\Delta x = \frac{W(4am)}{m}, \tag{4.35}$$

where W is the Lambert W-function defined by the implicit equation

$$x = W(x)\exp(W(x)). \tag{4.36}$$

Since $W(x) \sim \log(x)$ as $x \to \infty$, the size of the interval for the trapezoidal rule grows logarithmically as the number of quadrature nodes is increased. This property means that the small regions near the end-points are more densely resolved for larger m. However, in floating-point arithmetics, the point $\phi_{\mathrm{DE}}(x)$ for a sufficiently large x can be indistinguishable from the end-points of the interval $[-1, 1]$. Thus, with the optimal spacing (4.35), it is necessary to inactivate many nodes outside the "trimmed" intervals $[\epsilon_I, \alpha - \epsilon_I]$ and $[\alpha + \epsilon_I, \pi - \epsilon_I]$ with an appropriate cutoff ϵ_I. To avoid such inefficiency, the inverse of ϕ_{DE} is instead used to find the inverse images of $[\epsilon_I, \alpha - \epsilon_I]$ and $[\alpha + \epsilon_I, \pi - \epsilon_I]$, and then the trapezoidal rule is applied to the transplanted integrands over the entirely valid intervals. Due to the simplicity of the tanh-sinh transformation, its inverse is explicitly written as

$$\phi_{\mathrm{DE}}^{-1}(y) = \operatorname{asinh}\left(\frac{2}{\pi}\operatorname{atanh}(y)\right). \tag{4.37}$$

In our numerical experiments, quadrature nodes and weights in the formula (4.34) are precomputed using multiple-precision floating-point arithmetics.

Numerical Experiments

Following the previous works [26, 29], the two candidates are tested on the initial data (2.19), which corresponds to the instantaneous velocity

$$w_r(\alpha) = \frac{1}{4}\sin(2\alpha), \quad w_z(\alpha) = -\left(\frac{5}{12} + \frac{1}{4}\cos(2\alpha)\right). \tag{4.38}$$

Here, the variables r, z, γ and their derivatives are sampled on the 256-point Fourier grids in $[0, 2\pi)$, and the velocity (w_r, w_z) is approximated for those in $(0, \pi)$. Also, to implement open quadrature rules, all the periodic functions in Eqs. (4.14)(4.15) including $P - c_P J$ and γ'/r' are interpolated by evaluating their truncated Fourier series, as opposed to Nie and Baker [29] who uses quintic splines to reduce computational costs. On the other hand, the values of the time-independent factors $[J - (\alpha' - \alpha)^{-1}]$ in (4.16) are precomputed using multiple-precision floating-point arithmetics. For approximations of the complete elliptic integrals, the iterative algorithms described in [42] are mainly used. However, as already mentioned, the derivative $\partial\lambda/\partial\alpha'$ always vanishes at $\alpha' = \alpha$, which means that λ approaches $\lambda = 1$ (i.e. the singular point of K and E) in a quadratic manner. Such behavior of λ can be problematic for both quadrature rules because the accuracy of the iterative algorithms rapidly deteriorate as $\alpha' \to \alpha$. We avoid this problem by finding the following expansion of $\log\zeta = \log(1 - \lambda^2)$ with $\lambda^2 \le 1$:

$$\begin{aligned}
\log(1-\lambda^2) &= \log\left(1 - \sum_{k=0}^{\infty} \frac{(\lambda^2)^{(k)}}{k!}(\alpha' - \alpha)^k\right) \\
&= \log\left(\left|\sum_{k=2}^{\infty} \frac{(\lambda^2)^{(k)}}{k!}(\alpha' - \alpha)^k\right|\right) \\
&= 2\log|\alpha' - \alpha| + \log\left(\left|\sum_{k=2}^{\infty} \frac{(\lambda^2)^{(k)}}{k!}(\alpha' - \alpha)^{k-2}\right|\right),
\end{aligned} \tag{4.39}$$

where $(\lambda^2)^{(k)}$ is the k-th derivative of λ^2 with respect to α' evaluated at $\alpha' = \alpha$. In the above calculation, we have used $(\lambda^2)^{(0)} = 1$ and $(\lambda^2)^{(1)} = 0$, while $(\lambda^2)^{(2)}$ is non-zero as long as the relative spacing s_α is positive. Therefore, λ approaches $\lambda = 1$ no faster than quadratically provided s_α is appropriately controlled by the tangential velocity. Thus, combining Eq. (4.39) with Eqs. (4.1)(4.2), we can approximate $K(\lambda)$ and $E(\lambda)$ near $\alpha' = \alpha$ in terms of the logarithmic function with $|\alpha' - \alpha|$ and the smooth remainder. To switch

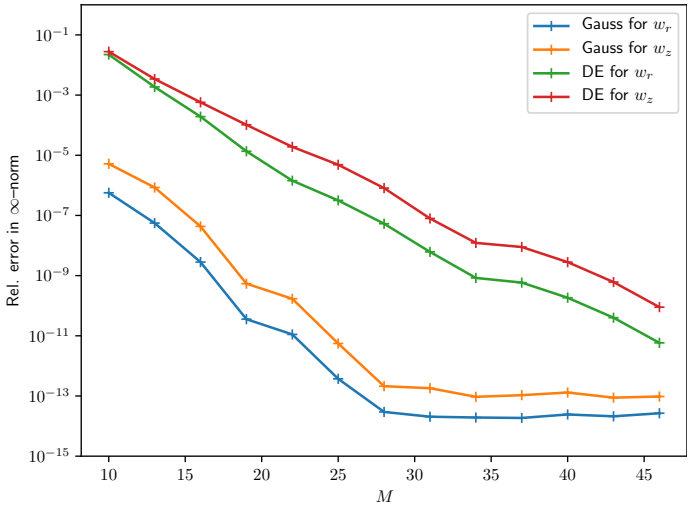

Figure 4.1: Convergences of quadrature rules applied to Eqs. (4.14)(4.15).

between the two different methods, the condition $(1 - \lambda^2) > \epsilon_\zeta$ is checked for some $\epsilon_\zeta > 0$. If this inequality holds, the iterative algorithms are used; otherwise, we use the approximations based on the local expansion (4.39). In practice, it turns out that the third-order approximation of the smooth remainder with $\epsilon_\zeta = 10^{-6}$ is enough for relative errors uniformly below 10^{-13} in the example (4.38). All the coefficients in Eqs. (4.1)(4.2) necessary for this purpose is given in Appendix A (see Eqs. (A.4)(A.5)).

Figure 4.1 shows convergences of the two candidates applied to the right-hand sides of Eqs. (4.14)(4.15). For each curve, numerical errors are plotted versus the size of quadrature rules in terms of the ∞–norm divided by the maximal value of the corresponding velocity. Since the regularized integrands are integrable over both $[0, \alpha]$ and $[\alpha, \pi]$, the integrals over $[0, \pi]$ are split as

$$\int_0^\pi f(\alpha, \alpha')d\alpha' = \int_0^\alpha f(\alpha, \alpha')d\alpha' + \int_\alpha^\pi f(\alpha, \alpha')d\alpha', \tag{4.40}$$

and a M-point quadrature rule is applied to each term after simple changes of variables. For the Gaussian quadrature rules for the Müntz systems (4.31), a superalgebraic convergence is clear for each velocity, and both error curves seem to reach the best accuracy at around $M = 34$ (10^{-14} for w_r and 10^{-13} for w_z, respectively). On the other hand, the convergence of the DE rule with $\epsilon_I = 10^{-15}$ is also superalgebraic in both cases, although it is somewhat

slower than the Gaussian rules and the same accuracy is achieved at around $M = 70$. This result is rather surprising because the regularized integrands should show singular behavior similar to (4.5) and the DE rule is capable of dealing with such difficulties at both end-points. Regarding this point, we speculate that large coefficients in the expansion (4.17) may cause the decay of the transplanted integrands to be slower near the axis of symmetry.

Composite Gaussian Quadrature Rules

In the experiments above, it is shown that the Gaussian quadrature rules for the Müntz systems (4.31) outperform the DE rule based on the tanh-sinh transformation (4.32). Unfortunately, however, neither of the schemes is practical by itself for simulating long-time motion of axisymmetric vortex sheets with surface tension. That is, as explained earlier, computing generalized Gaussian quadrature rules for large systems is too expensive, while even a very large DE rule can easily break down in the course of a simulation, presumably due to the sensitivity of the method to oscillatory functions [38]. To address this problem, we develop a composite quadrature scheme based on the Gaussian quadrature rules for the systems (4.31) and the classical Gauss-Legendre rules for polynomials. In this strategy, after equally dividing $[0, \pi]$ into M subintervals, the 97-point rule for the system (4.31) (i.e. $k^* = 65$) is applied in the two closest to the singularity, and the 16-point Gauss-Legendre quadrature rule is used in the others. For the example (4.38), this composite scheme with $M = 128$ achieves relative errors uniformly below 10^{-13} for both w_r and w_z. Moreover, one can show that the integrand B_z has the limits

$$B_z(\alpha, \alpha', t) = \frac{\gamma'}{2} \frac{r'^2}{(\xi^2 + r'^2)^{\frac{3}{2}}}, \tag{4.41}$$

for $\alpha = 0, \pi$. Thus, the integrand B_z is regular at the end-points, and the values of r, z, and γ for the 16-point Gauss-Legendre quadrature rule can be reused to compute the velocity on the axis of symmetry. This special approximation scheme is used in Chapter 6 for the convergence study of a numerical method involving the approximation (3.25).

Chapter 5

Numerical Methods

We numerically solve the initial value problem of Eqs. (2.12)(2.15)(2.16) with the normal velocity $U = \mathbf{W} \cdot \mathbf{n}$ and the tangential velocity V specified in Chapter 3. Our numerical method consists mainly of spatial discretization, evaluations of the guideline function GL, and temporal discretization compatible with the approximation (3.25).

5.1 Spatial Discretization

In our computations, the dynamical variables $(\theta, s_\alpha, \gamma)$ are sampled at N points equally spaced in the extended parameter space $[0, 2\pi]$:

$$\alpha_j = jh, \quad h = \frac{2\pi}{N}, \quad j = 0, 1, \ldots, N-1, \tag{5.1}$$

and all the derivatives and anti-derivatives are evaluated using the standard fast Fourier transform (FFT). Except for computing a reference solution of the convergence study in Chapter 6, the principal-value integrals (2.9) and (2.10) are discretized by the third-order uniform approximation by Nitsche [26] with 8193 points. For this purpose, the values of (r, z, γ) between the grid points (5.1) are obtained by the FFT-based Fourier interpolation after the reconstruction from (θ, s_α). In our code, evaluations of the integrands in (2.9) and (2.10), including the iterative algorithms for K and E [42], are parallelized on a single NVIDIA Tesla P100, a Graphical Processing Unit (GPU) for scientific computing in the double-precision floating-point arithmetics. Also, the direct summation after the integrand evaluations is performed with the warp-shuffle reduction algorithm [43] on the same GPU.

5.2 Evaluation of Guidelines Functions

Next, we apply the trapezoidal rule to the Fourier coefficients (3.10) after the change of variables (3.11):

$$\hat{f}(k) \approx \frac{h}{L_p} \sum_{j=0}^{N-1} (f(s(\alpha_j)) s_\alpha(\alpha_j)) e^{-2\pi i \frac{s(\alpha_j)}{L_p}}. \tag{5.2}$$

Unfortunately, these discrete sums cannot be directly computed using the standard FFT, because the nodes $s(\alpha_j)$ are redistributed non-uniformly in $[0, L_p]$ by mesh refinement. Instead, we can use the non-uniform fast Fourier transform (NUFFT), which is an $\mathcal{O}(N \log N)$ algorithm approximating the following types of sums to a prescribed relative accuracy ϵ_{rel}:

$$\text{(Type-1)} \quad \hat{f}_k = \sum_{j=0}^{N-1} f_j e^{-ikx_j}, \quad k = -\frac{M}{2}, \dots, \frac{M}{2} - 1, \tag{5.3}$$

$$\text{(Type-2)} \quad f_j = \sum_{k=-\frac{M}{2}}^{\frac{M}{2}-1} \hat{f}_k e^{ikx_j}, \quad j = 0, 1, \dots, N-1. \tag{5.4}$$

It is easy to see that the formula (5.2) naturally fits in the framework of the Type-1 NUFFT (5.3). On the other hand, once the Fourier coefficients of GL are obtained, it can be interpolated back to the non-uniform grid $s(\alpha_j)$ using the Type-2 NUFFT (5.4). Here, we note that there are several implementations of the NUFFT algorithms for general purposes, including CMCL NUFFT [44], NFFT3 [45], and FINUFFT [7]. In our code, we employ FINUFFT with a few cores of Intel Xeon Gold 6136, for, to our knowledge, it is currently the fastest library parallelized with OpenMP. Also, it should be noted that the Type-1 NUFFT itself is not related to any quadrature rules and simply approximates sums of a particular form. In our scheme, the coefficients $s_\alpha h$ serve as quadrature weights compatible with the non-uniform nodes $s(\alpha_j)$ that evolve in time, which automatically addresses this issue.

Our practical procedure for evaluating GL is as follows. Firstly, we decide the largest wavenumber $k_{\max}$ of the Fourier coefficients $\hat{\kappa}_z(k)$ computed for the mesh refinement purpose. This is equivalent to choosing a target spatial resolution in terms of the uniform mesh that we aim to achieve with a non-uniform one realized by our mesh refinement. Therefore, the number $k_{\max}$

should be related to the parameter δ_R in (3.21) so that the target resolution is always no finer than the best possible local resolution determined by δ_R. Secondly, if we assume that our scheme is working ideally, the locally refined mesh resolves κ_z successfully, whereas complex exponentials, which oscillate uniformly in $[0, L_p]$, can be underresolved for sufficiently large k. To resolve both κ_z and those complex exponentials, the functions κ_z, s_α, and s are interpolated by the truncated Fourier serires to an upsampled grid with N_{up} points in $[0, 2\pi]$, and then the coefficients $\hat{\kappa}_z(k)$ are computed using the Type-1 NUFFT. Thirdly, once the coefficients $\hat{\kappa}_z(k)$ are obtained for $|k| \leq k_{\max}$, the curvature κ_z as a function of the arclength and its Hilbert transform are computed by inverting the corresponding Fourier coefficients with the standard FFT, and the analytic envelope $E_r[\kappa_z]$ is evaluated in $[0, L_p]$. Lastly, we transform $E_r[\kappa_z]$ back to the Fourier space, apply the Gaussian filter, and finally interpolate the resulting GL to the non-uniform grid $s(\alpha_j)$ using the Type-2 NUFFT. Since each step involves $\mathcal{O}(N)$ and $\mathcal{O}(N \log N)$ operations only, additional costs for our mesh refinement strategy are $\mathcal{O}(N \log N)$.

5.3 Temporal Discretization and Filtering

We evolve the dynamical variables $(\theta, s_\alpha, \gamma)$ using the classical fourth-order Runge-Kutta method. With surface tension, it is well-known that high-order terms in κ_α introduce stiffness into the governing equations and the stepsize Δt is required to satisfy a severe stability constraint. In the case of axisymmetric vortex sheets, this constraint is known to be $\Delta t \leq C \Delta s_{\min}^{3/2}$, where $\Delta s_{\min}$ is the minimum distance between computational points in the symmetry plane. In this thesis, we follow NS04 and try to satisfy the condition with $C = 2.5$ as long as possible. For a general time-independent R, a semi-implicit scheme that removes the stiffness has been developed by HLS97, and an extension of the method to general cases is a direction of future works.

For the formula (3.25), we use $\tau = \tau_i$ at the i-th Runge-Kutta stage with

$$\tau_1 = \Delta t, \quad \tau_2 = \tau_3 = \frac{1}{2}\Delta t, \quad \tau_4 = \Delta t. \tag{5.5}$$

Combining these coefficients with the property (3.24), we can perform time-stepping by the classical Runge-Kutta method without any interpolation technique in the temporal direction. It is not clear that the coefficients used in NS04 are the same as our choice, and there may be some alternative

values. A drawback of this procedure is that it amounts to introducing a highly oscillatory delay $\tau(t)$ inevitably associated with Δt and may affect the convergence of our temporal discretization. This issue is carefully discussed in Chapter 6.

Also, the spectral filter introduced by Krasny [17] is applied to numerical solutions at every time step. This technique removes all Fourier coefficients whose magnitudes are below a cut-off level ϵ_K, and it is originally used to control unphysical growths of round-off errors due to the Kelvin-Helmholtz instability in the zero surface tension case. In the present formulation, another source of noises is the principal curvature κ_r, which is a quotient of two functions that vanish on the axis of symmetry. Since Eq. (2.12) involves the derivative of this function, large noises can be introduced to numerical solutions and grow under, for example, the Kelvin-Helmholtz instability. The Krasny's filter is also expected to control the latter problem, as demonstrated in NS04.

Chapter 6

Numerical Results

Now we show some numerical results to validate the numerical method described in Chapter 5. In the following computations, the parameters for our mesh refinement scheme are given by

$$a = 20, \quad d = 5, \quad \delta_R = \frac{1}{8}, \quad k_{\max} = 8\left(\frac{N}{2}\right), \quad N_{\mathrm{up}} = 32N, \tag{6.1}$$

with the relative accuracy $\epsilon_{\mathrm{rel}} = 10^{-15}$ for the NUFFT algorithms. The other parameters N, Δt and ϵ_K are specified in each section.

6.1 Construction of Uniform Parametrization

As a limitation of the definition (3.21), it is required to construct an initial condition in the uniform parametrization before any time-stepping is performed. There are at least two ways to accomplish this step. The first is to determine the total length L (or equivalently the relative spacing s_α constant in α) and the functions θ and γ that are assumed to be in the uniform representation. This approach is cleverly used by Almgren [46] to design initial shapes of Hele-Shaw bubbles that can lead to finite-time singularities. The second is to find the uniform parametrization of a given initial condition using some numerical techniques. Fortunately, the latter approach can be implemented by an immediate application of the ideas described in Chapter 5. Remember that the formula (5.2) is the trapezoidal rule applied to a smooth periodic function of the variable α, which is known to be spectrally accurate. On the other hand, the arclength parametrization is a special case

of the uniform ones whose domain is $[0, L_p]$. Hence, by inverting the approximate coefficients (5.2) via the standard FFT, we expect to obtain a function represented in the uniform parametrization with spectral accuracy. To our knowledge, this procedure is distinctly different from the existing methods designed for the same purpose. For instance, Baker and Shelley [47] suggests an iterative scheme based on the Newton's method, which searches for a set of values α_j corresponding to $s(\alpha_j)$ equally spaced in $[0, L_p]$. In another direction, Mikula and Ševčovič [48] proposes the concept called *asymptotically uniform parametrization*, which can define a "time-evolving" method that fixes $U = 0$ and evolves a plane curve solely by the tangential velocity V until the relative spacing s_α converges to a constant. Our method needs neither the Newton's method nor temporal discretization, and it is completely non-iterative.

To justify the argument above, our initialization algorithm is tested on the following example in polar coordinates (η, ϕ):

$$\eta(\phi) = 1 + \epsilon_P P_2(\cos\phi), \quad \phi \in [0, 2\pi]. \tag{6.2}$$

Here, ϕ is the polar angle, η is the radius as a function of ϕ, and P_2 is the Legendre polynomial of order two. This special choice, which is presented in [49], corresponds to the zero-velocity state of a periodic solution to the linearized problem in [50]. The representation in the polar coordinates allows to compute the "inverse" mapping $(r, z) \mapsto \phi$ and check the accuracy of numerical results against the explicit data (6.2), although our method is also applicable to smooth closed curves given in Cartesian coordinates.

Following HLS94, we first compute the curvature κ_z and the relative spacing s_α from (6.2), and find the representation of κ_z in the uniform parametrization by our initialization algorithm. Then, with $s_\alpha = L_p/2\pi$, the derivative $\theta_\alpha = s_\alpha \kappa_z$ is integrated to obtain θ, which is followed by the reconstruction of (r, z). In Fig. 6.1, the plane curve (6.2) and the convergence of the scheme are shown for $\epsilon_P = 2/7$. As shown in Fig. 6.1(a), it has the variable radius η and therefore its parametrization is non-uniform. Next, in Fig. 6.1(b), numerical errors in r and z are plotted versus N in terms of the ∞–norm divided by the maximal value of each function. The exponential convergence of the trapezoidal rule is clear, and each graph reaches a level slightly above 10^{-15} for $N \geq 150$. In fact, we do not perform a construction of the uniform parametrization for the initialization purpose, because the conditions (2.17) and (2.19) are uniform by definition. Instead, our algorithm

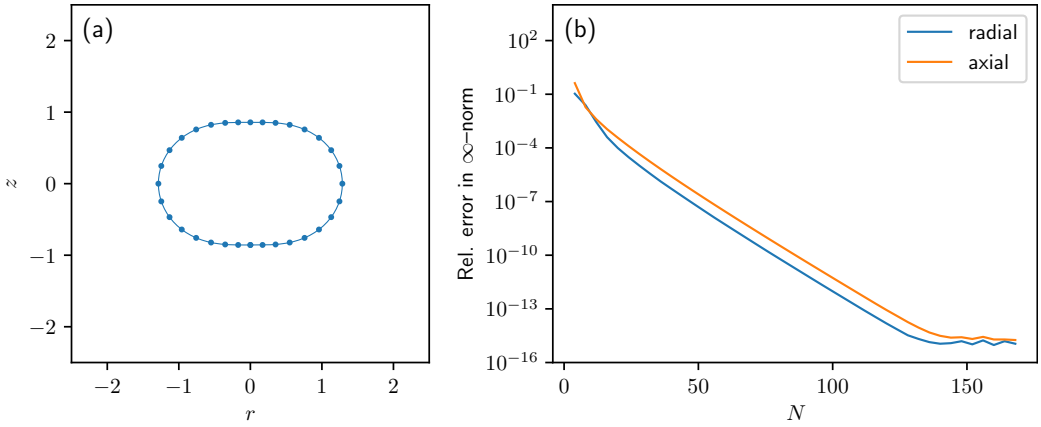

Figure 6.1: (a) Interface position of test problem (6.2) in r–z plane, (b) exponential convergence of initialization algorithm based on inverting approximate coefficients (5.2).

is effectively used in the convergence study of the time-stepping with the approximation (3.25), which requires to remove effects of mesh refinement for comparisons between two solutions with different tangential velocities.

6.2 Capillary Pinch-off

Our numerical method is first tested on the pinch-off problem (2.17) with $N = 2048$, $\Delta t = 5 \times 10^{-5}$, and $\epsilon_K = 10^{-11}$. Figure 6.2 plots the numerical solutions in the r–z plane at indicated times, including the symmetric image in $r < 0$. To clearly show arrangements of computational points, in each figure the solid line is drawn at the the full resolution and every 16th point is plotted again as a dot. At $t = 0.50$, the droplet starting from a sphere is axially deformed and acquires a capsule-like shape. Since it is still relatively close to a sphere, the effect of mesh refinement is only slightly visible as sparseness near $z = 0$. At $t = 1.00$, the capsule-like droplet is further elongated along the z–axis, and now it has developed two round ends connected by a thick rod. At this moment, the rod in the middle is almost straight near $z = 0$, while geometry is relatively simple around the end-points $\mathbf{X}(0, t)$ and $\mathbf{X}(\pi, t)$. For these simplicities, computational points are beginning to accumulate near the junctions between the rod and the round ends, as clearly

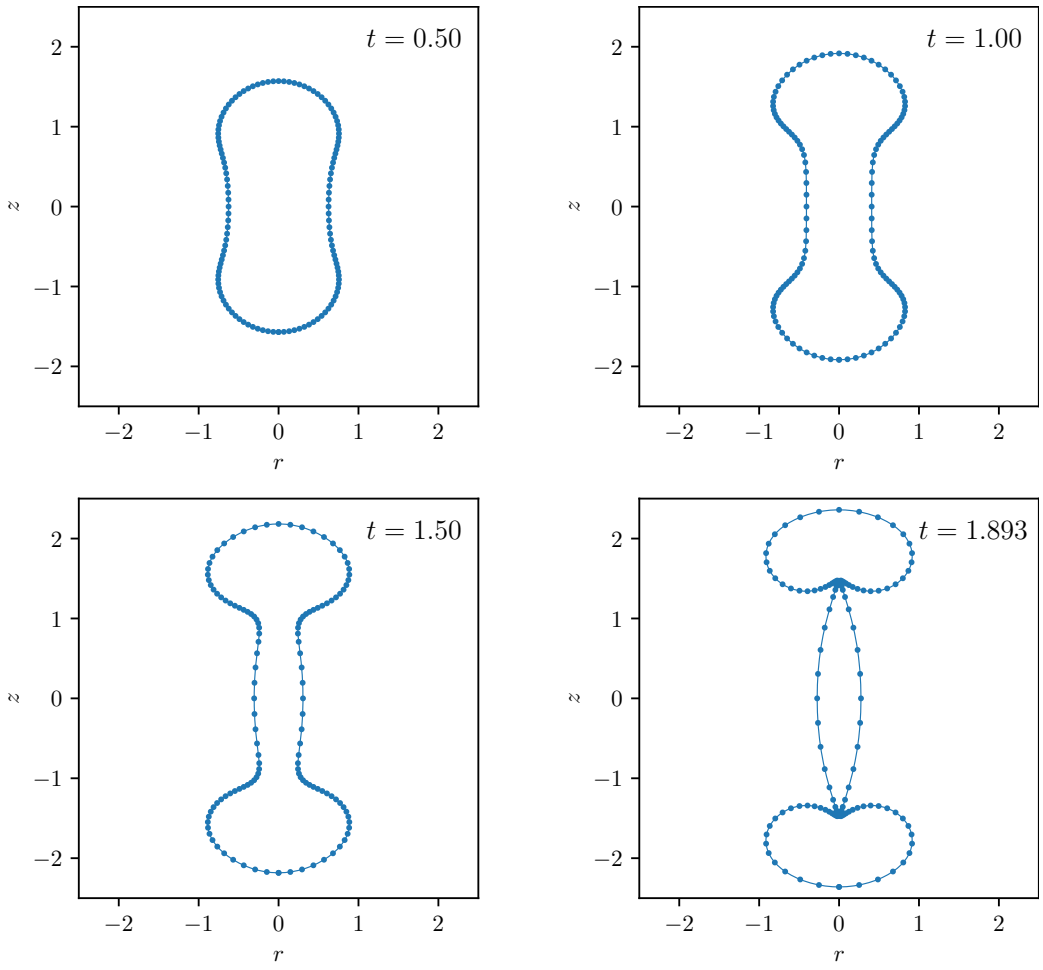

Figure 6.2: Snapshots of interface position at indicated times for pinch-off problem (2.17).

seen in the corresponding figure. Almost the same argument applies to the solution at $t = 1.50$. Here, the radius of the rod is no longer uniform, and two isolated points of the minimum neck radius are formed near the junctions, implying where pinch-off is about to occur. At $t = 1.893$, which is just before noises become visible in the numerical solution, the minimum neck radius has rapidly decreased and the droplet is forming two end-droplets at the top and bottom along with a sharply elongated satellite droplet in between. Also, as discussed in Chapter 2, overturning is found in each pinch-off region, and it

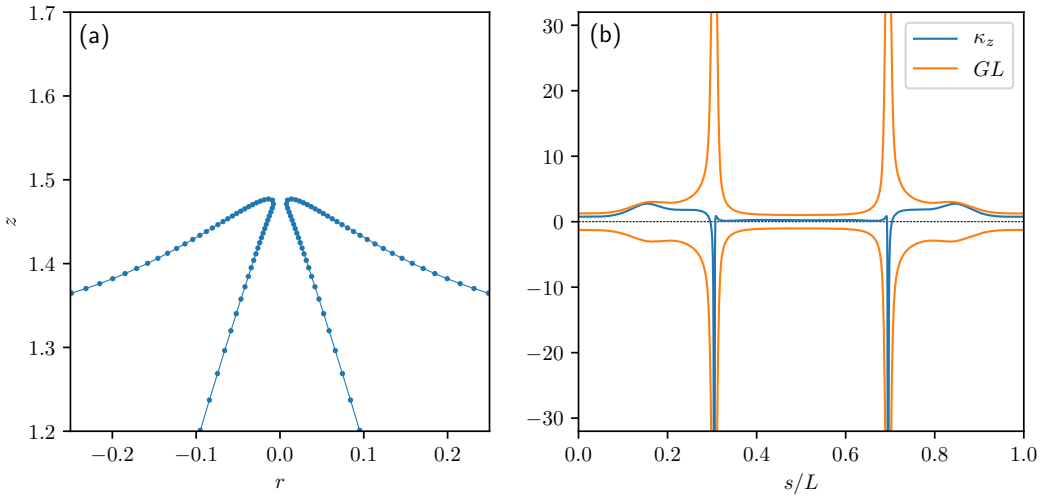

Figure 6.3: Interface profile for pinch-off problem (2.17) at $t = 1.893$: (a) closeup of pinch-off region with every 4th point plotted as dot, (b) plots of κ_z and GL.

develops the so-called cone-crater structure intensively studied by NS04. For reference, this GPU-accelerated simulation took approximately 1.25 hours with a single CPU core and one hour with two cores. We could not find significant speed gain from further increasing the number of CPU cores, which is presumably because the orders of $k_{\max}$ and N_{up} were relatively small compared to the main target of the parallelized NUFFT algorithms (see [7] for details). The same simulation was performed with the uniform parametrization and took roughly 10 minutes, although the numerical solution at around $t = 1.89$ was contaminated by noises at the highest wavenumber.

In Fig. 6.3(a), we show a closeup of the upper pinch-off region at $t = 1.893$. As easily seen in the figure, a small region containing the shrinking neck is densely resolved by our mesh refinement scheme, and the minimum value of s_α is six times smaller than that of the uniform parametrization. This refinement is roughly 1.3 times coarser than that of HLS97, and two times than that of NS04. In Fig. 6.3(b), the curvature κ_z and the corresponding GL are shown for the same t. As expected, the procedure outlined in Chapter 5 successfully generates a simple and strictly positive GL from the curvature κ_z with two significantly sharp peaks. Here, note that the locality of mesh refinement can be improved by increasing the parameter a in (3.19) at the cost

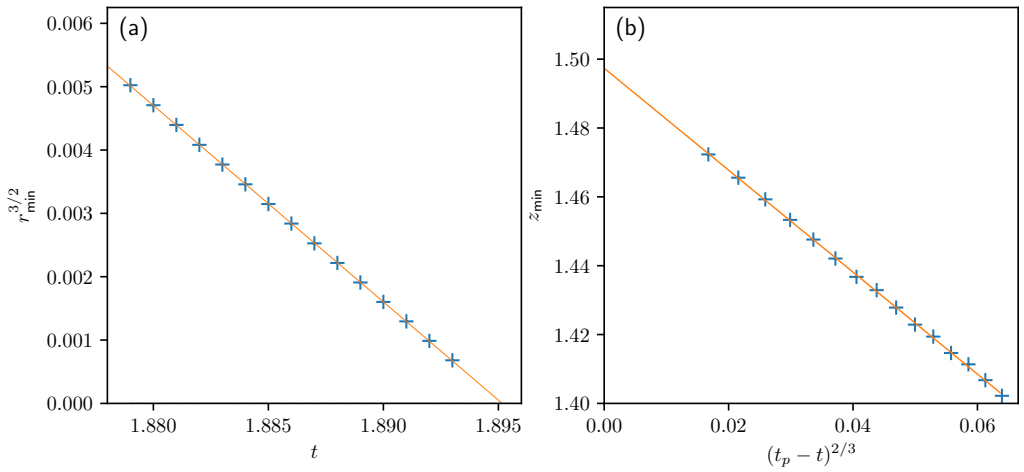

Figure 6.4: Confirmation of scaling law (2.18) for pinch-off problem (2.17): (a) $r_{\min}^{3/2}$ vs t, (b) $z_{\min}$ vs $(t_p - t)^{2/3}$.

of the smoothness of GL. An ideal scheme should be capable of updating the value of a adaptively in the course of simulations as high-curvature regions develop. Unfortunately, we have not found any indicator that can evolve $a(t)$ in a differentiable manner without any a priori information, and the fixed parameters in (6.1) have been obtained by trial and error. However, once we know a set of parameters that works properly, it can often be reused for other initial conditions, as we see in the second example (2.19).

Next, we confirm the scaling law (2.18) using our numerical results. The procedure is essentially the same as in NS04. Firstly, in Fig. 6.4(a), we plot $r_{\min}^{3/2}$ versus t and fit a straight line to the data points. As one can easily see, the fitted line clearly explains the linear behavior of $r_{\min}^{3/2}$, which suggests that the solution is in the self-similar regime. Secondly, by extrapolating the line to $r_{\min}^{3/2} = 0$, we obtain an estimate $t_p \approx 1.8951$, which is slightly smaller than $t_p \approx 1.89523$ obtained in NS04. Thirdly, the coordinate $z_{\min}$ is plotted in Fig. 6.4(b) as a function of $(t_p - t)^{2/3}$ using the value of t_p estimated at the previous step, and then another straight line is fitted to the data points. Although it is not as clear as for $r_{\min}^{3/2}$, it is still reasonable to conclude that the results are well explained by the fitted line. Again, by extending the line to $(t_p - t)^{2/3} = 0$, we obtain an estimate $z_p \approx 1.4973$,

while that by NS04 is $z_p \approx 1.49839$. From these results, we believe that our simulation with $N = 2048$ resolves the singularity formation slightly better than one by NS04 with the uniform parametrization and $N \approx 8000$. However, it should be also pointed out that the deviations of our estimates from those in NS04 are arguably due to the fact that our mesh refinement scheme fails to continue simulations at further smaller length-scales, where simple universal scalings such as (2.18) can be distinguished from more complicated situations including bubble collapse dominated by inertia [51] and droplet formations affected by weak viscosity [52]. The failure of our simulation is attributed mainly to the lack of an adaptive stepsize control, which is required to handle large interfacial velocity near singularity formations as well as the stiffness $\Delta t \leq C\Delta s_{\min}^{3/2}$ that becomes more severe as the spatial resolution is improved. This drawback is because of the introduction of the time delay τ in (3.25) linked to the stepsize and the classical Runge-Kutta method, which prevents us from updating Δt in a meaningful manner. Regarding this point, a promising strategy may be to use some interpolation technique in the temporal direction so that the delay τ can be untied from Δt and fixed at a sufficiently small value. Such flexibility may also allow to use more stable time-integration schemes than the classical Runge-Kutta method. We hope to address this issue in future investigations.

6.3 Convergence Study

NS04 justifies the controversial approximation (3.25) by showing that changing the resolution N or the parameter $\delta_{\max}$ in (3.7) does not affect the results in their figures similar to Fig. 6.4. In this thesis, we aim to verify in a more direct way that the time-stepping involving (3.25) actually converges faster than $\mathcal{O}(\Delta t)$. Before doing any special trick, we first perform a standard convergence study with the pinch-off problem (2.17) and the time $t = 0.50$ (see Fig. 6.2), where solutions with various Δt are compared in $[0, \pi]$ against an "exact" solution obtained with a sufficiently small stepsize. Here, to weaken the stiffness $\Delta t \leq C\Delta s_{\min}^{3/2}$, the number N is reduced to 256, and the "exact" solution is computed with $\Delta t = 10^{-5}$ and $\epsilon_K = 10^{-14}$. For large Δt that still violate the constraint, the instability typically appears as a rapid growth of the Fourier coefficients of numerical solutions at high wavenumbers. This fact is numerically demonstrated by HLS94 for two-dimensional vortex sheets with surface tension, and the same phenomenon should be seen

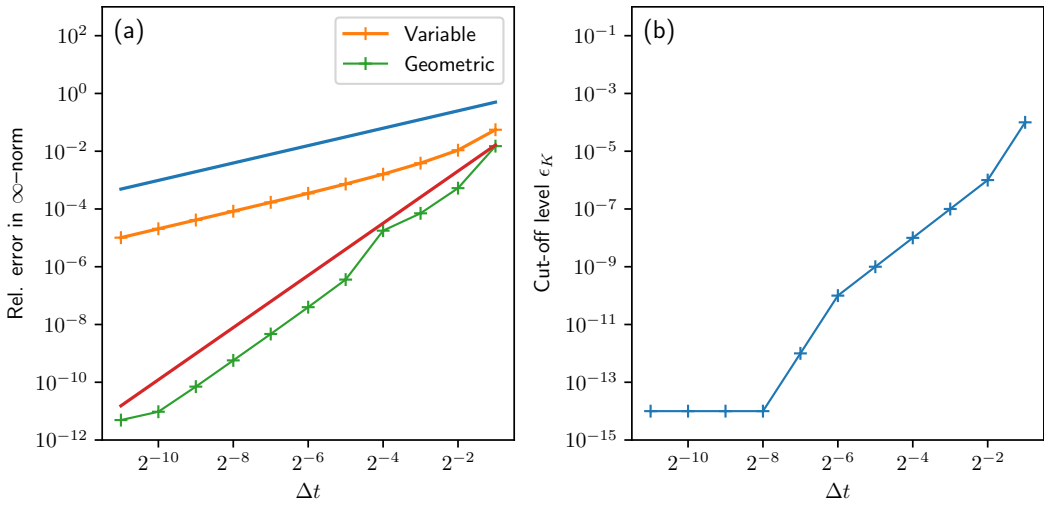

Figure 6.5: Convergence of time-stepping with approximation (3.25): (a) plots of errors measured as relative ∞–norm, (b) correspondence between stepsize Δt and filter level ϵ_K.

in the axisymmetric case. To continue simulations for such large Δt, we control the growth of the Fourier coefficients by adjusting the filter level ϵ_K. In Fig. 6.5(a), we plot errors in the mapping $\mathbf{X}$ measured as the ∞–norm divided by the maximum value of $|\mathbf{X}(\alpha_j, t)|$, and the correspondence between Δt and ϵ_K is shown in Fig. 6.5(b). As seen in Fig. 6.5(a), the error curve for $\mathbf{X}$ (denoted by "Variable" in the legend) is parallel to a linear function (blue line) and the convergence rate is apparently $\mathcal{O}(\Delta t)$. From this result, one may be tempted to conclude that the order of the classical Runge-Kutta method is completely lost. However, noting that a change in the stepsize Δt can alter the relative spacing s_α linearly through the approximation (3.25) with τ_i given in (5.5), we still hesitate to eliminate the possibility that the true convergence rate may be hidden behind the $\mathcal{O}(\tau)$ behavior of (3.25).

From this point of view, we repeat almost the same convergence study but with another "exact" solution. Note here that the initialization technique based on inverting (5.2) can be also used to remove effects of mesh refinement and transform a computed solution to its arclength parametrization. Since the shape of an evolving curve is expected to be independent of its tangential velocity V, this observation motivates us to compare results from our simulations in a canonical form, which is the arclength parametrization in

the present case, against a reference solution obtained by a more reliable numerical method. To compute such a quality solution, the pinch-off problem (2.17) is solved again by the classical Runge-Kutta method with $N = 256$, $\Delta t = 10^{-5}$ and $\epsilon_K = 10^{-14}$, but using the tangential velocity (3.6). Namely, the uniform parametrization of the initial condition (2.17) is maintained during the entire simulation, and the approximation (3.25) is not involved in this special case. Furthermore, in pursuit of better accuracy, the regularized Biot-Savart integrals (4.14) and (4.15) are discretized by the composite Gaussian quadrature rule developed in Chapter 4 with $M = 128$. In Fig. 6.5(a), an error curve obtained after removing the potential artifacts (denoted by "Geometric") is plotted with a theoretical $\mathcal{O}(\Delta t^3)$ line (red line). As opposed to the result above, the convergence rate here is clearly superlinear and estimated to be at least $\mathcal{O}(\Delta t^3)$, which strongly suggests that the numerical solutions with our mesh refinement converge, at least in a geometric sense, to the reference solution faster than the approximation (3.25), although some order reduction may be occurring due to the fast oscillation of τ_i.

6.4 Bag Breakup

Next, the performance of our numerical method is further examined in its application to the axisymmetric bag breakup (2.19) with the same N, Δt, and ϵ_K as for the pinch-off problem. Again, Figure 6.6 plots the numerical solutions in the r–z plane (including $r < 0$) at indicated times, and every 16th point is plotted as a dot after drawing the solid line at the the full resolution. Also, since we do not evolve the end-point $\mathbf{X}(0, t)$ in this simulation, the interface position in each figure is reconstructed with $\mathbf{X}(0, t) = (0, -1)$. At $t = 1.00$, the droplet, which is initially a sphere, has developed a small indentation at the top and the inner region is no longer convex. The effect of mesh refinement is not evident here because no complex geometry is found in the interface. At $t = 2.50$, as the indentation further develops, the droplet begins to acquire a bowl-like shape whose edge is bent toward the axis of symmetry. Now, computational points weakly cluster near the two round corners of the edge, and consequently some sparseness is found away from those small regions. At $t = 4.00$, a large volume of the inner fluid has flowed into the edge region and the bottom of the bowl has become thinner. At $t = 4.90$, which is just before the numerical solution is contaminated by

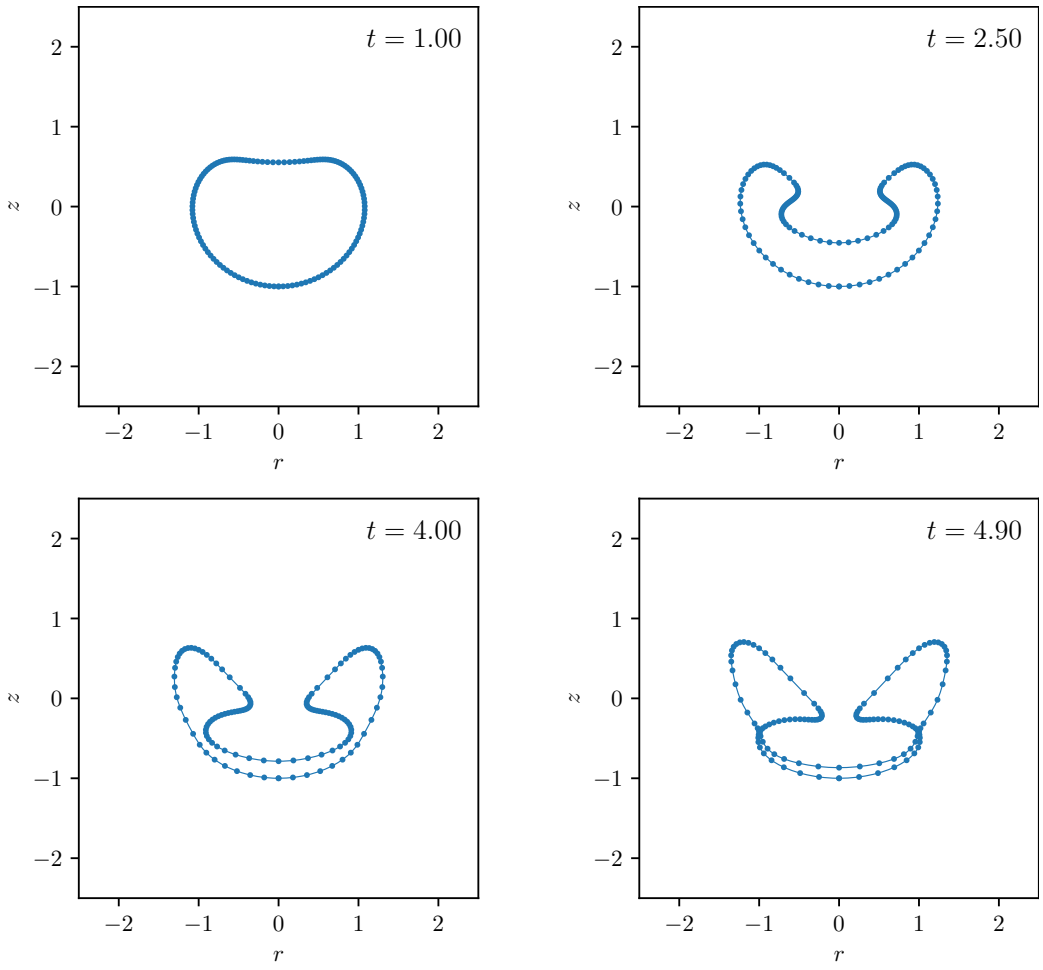

Figure 6.6: Snapshots of interface position at indicated times for axisymmetric bag breakup (2.19).

noises, the fluid interface is about to collide itself at the point connecting the edge and the bottom. As one can see, most of computational points are now devoted to resolving the two corners of the edge and the small region around the self-intersection.

The topological change shown in Fig. 6.6 should be considered qualitatively different from that in Fig. 6.2. In the case of bag breakup, the droplet is about to break into one torus-like component and one simply-connected component, whereas the symmetric pinch-off seems to form three simply-

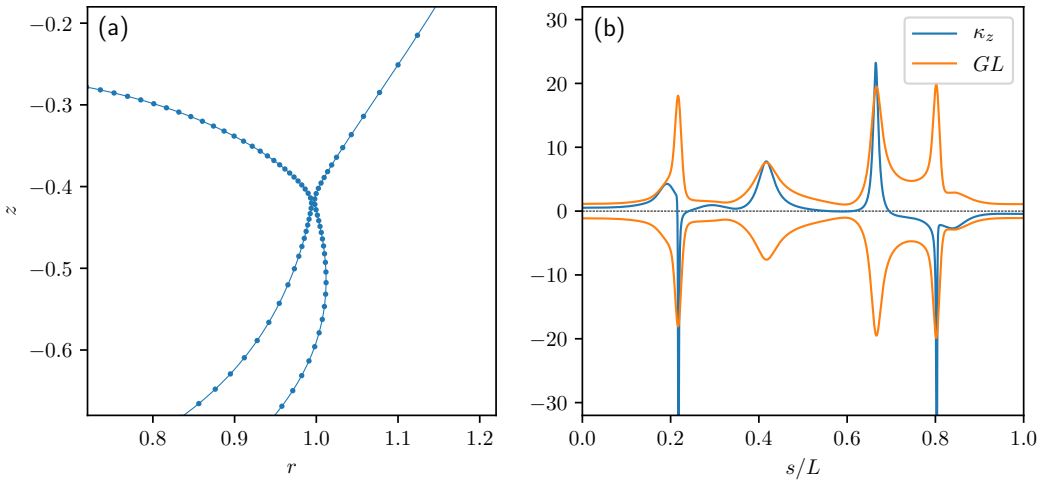

Figure 6.7: Interface profile for axisymmetric bag breakup (2.19) at $t = 4.90$: (a) closeup of self-intersection region with every 4th point plotted as dot, (b) plots of κ_z and GL.

connected ones. In Fig. 6.7(a), we show a closeup of the region near the point of the self-intersection at $t = 4.90$. As opposed to capillary pinch-off, overturning or a cone-crater structure is not observed in this case, and the fluid interface has two corners facing each other. This structure is more similar to those found in, for example, HLS97 and Burton and Taborek [5]. For the same t, the curvature κ_z and the corresponding GL are shown in Fig. 6.7(b). In this case, the solution forms two high-curvature regions away from the point of the self-intersection, which precludes applications of mesh refinement based on the prescribed guideline (3.7). As expected, our method succeeds in generating a simple and strictly positive GL from the curvature κ_z with four peaks with different magnitudes. Here, the relative spacing s_α is roughly two times smaller for the smallest peak than that of the uniform parametrization, and 3.5 times smaller for the others three. On the other hand, a drawback of mesh refinement based on the analytic envelope is found in the interval between the two right-most peaks in Fig. 6.7(b). In the function GL, the two adjacent peaks are "bridged", which is again presumably due to the low-frequency nature of the operator E_r, and our mesh refinement scheme overestimates the complexity of a region where the curvature κ_z is small and smooth (see Fig. 6.6). This phenomenon is not because of the effect

of the Gaussian filter. In fact, this bridged function is found "before" applying any smoothing filter, and therefore inherent to the use of the analytic envelope.

Chapter 7

Conclusion

In this thesis, a novel mesh refinement scheme is proposed for the vortex sheet formulation of inviscid droplet dynamics with axial symmetry. The method is based on signal processing using the Fourier coefficients of the curvature in the r–z plane as a function of the arclength, which are expected to be invariant under a change of parametrization with a few conditions. A combination of the analytic envelope and the subsequent Gaussian filter extracts an outline of the curvature profile and enables to automatically detect two kinds of singularity formations associated to self-intersections of the surface of a droplet. With the help of the non-uniform fast Fourier transform, an emerging tool in computational harmonic analysis, additional costs for discretizing the Fourier coefficients with the arclength variable are reduced to $\mathcal{O}(N \log N)$, which underlies the efficiency of the present scheme. Also, we suggest a non-iterative construction of the uniform parametrization for periodic plane curves, and use it to confirm, at least in a geometric sense, a superlinear convergence of the time-stepping procedure with the approximation (3.25) introduced by NS04. Moreover, to compute an accurate reference solution in the convergence study, a direct approximation scheme for the axisymmetric Biot-Savart integrals is developed based on a new regularization technique using singular periodic functions and the generalized Gaussian quadrature rules for Müntz systems as minimizers to a class of nonlinear least-squares problems.

There are several important directions for future works in relation to limitations of the current method. Firstly, as pointed out in Chapter 6, our mesh refinement scheme is capable of detecting two types of singularity formations, but the lack of an adaptive stepsize control precludes sufficient

resolutions of their profiles at smaller time- and length-scales where the famous 2/3 law (2.18) can be distinguished from other scalings. In addition to the difficulty near self-intersections, HLS94 reports that the "shadow" of the Moore's singularity and its saturation can lead to fast changes in solutions and cause sudden drops in overall accuracy. Moreover, Ambrose [53] points out using their model problem that nearly-singular behavior unrelated to any self-intersection can appear even in the non-zero surface tension case. These facts strongly suggest that flexibility in controlling the stepsize during simulations is necessary in simulations of vortex sheets with suraface tension. Unfortunately, however, it is not trivial to change the stepsize adaptively in the proposed method because of the formula (3.25) with τ_i given in (5.5). To eliminate this restriction, it may be a key to gain more insights into the approximation as a delay term in the formulation. That is, regarding the problem as integro-differential equations with a delay, one could employ a time integrator with dense outputs or a polynomial interpolation in the temporal direction, which allows to fix the value of τ at a sufficiently small value and remove the oscillations of τ_i in (5.5). A more ambitious goal would be to follow the style of Leppinen and Lister [3], which separates mesh refinement from time-steppings and advects computational points with a well-known tangential velocity not involving the formula (3.25). In this direction, it is required to perform remeshing at the beginning of each time step based on some numerical optimization or a "time-evolving" method with the zero normal velocity (i.e., $U = 0$). Once an adaptive stepsize control is enabled, the improved numerical method should be validated by reproducing, for example, the bubble collapse dominated by inertia [51], where some logarithmic corrections in its self-similarity are found at very small length-scales, and then by explaining experimental results such as droplet formations affected by weak viscosity [52] with numerical simulations. As a model for the latter challenge, the boundary integral formulation with weak viscous effects suggested by Lundgren and Mansour [54] is a promising candidate.

Secondly, for example, a hanging bridge between two peaks of the guideline function GL, which is found in the case of bag breakup, results in some inefficiency of our mesh refinement scheme. This drawback motivates us to seek an alternative technique in signal processing that replaces the analytic envelope employed in the present work. However, it is obvious that the current method heavily relies on differentiability of the regularized analytic envelope (or equivalently, the Hilbert transform) with respect to the time variable, which prevents us from using modern concepts in signal pro-

cessing. This is the main reason why following Leppinen and Lister [3] is more ambitious and desirable than interpolating numerical solutions in the temporal direction. Namely, by perfoming remeshing and time integration independently, the guideline function and associated parameters no longer need to be updated in a differentiable manner, because those are checked at the very beginning of each time step only and never affect the convergence of discretization in time. Thus, the resulting mesh refiement scheme should be able to use a wide variety of signal processing approaches and acquire further adaptivity in adjusting the locality of mesh distributions. Needless to say, the convergence of such a scheme can be confirmed in a geometric sense only, whereas the numerical method implemented in this thesis may actually converge in the pointwise manner. Even in the case, the procedure of the convergence study in Chapter 6 should be valid without any modification.

Lastly, the existence of non-trivial solutions without singularities is open for the axisymmetric vortex sheets with surface tension. Regarding this point, Lundgren and Mansour [54] reports that an inviscid droplet with axial symmetry can break up even after oscillating several times, and the weak viscosity in their model is in fact introduced to avoid wild behavior due to the lack of a damping effect. On the other hand, in two-dimensional cases with a periodic boundary condition, Amborse and Wilkening [55] numerically discovers time-periodic solutions with some symmetry to the fully nonlinear problem based on a quasi-Newton method that minimizes the differences between initial conditions and the corresponding numerical solutions at a target period. As an extension of their work, an interesting problem is computations of time-periodic solutions, which are naturally global in time, to the initial value problem considered in this thesis, possibly with the linealized periodic solutions (6.2) as initial inputs. For this purpose, the composite Gaussian quadrature rule developed in Chapter 4, which is particularly efficient and accurate for relatively small N, should be useful, because a moving boundary showing nearly time-periodic motion is often far away from self-intersections and sufficiently resolved with a small number of discrete points.

Appendix A

List of Local Expansions

Asymptotics for P and J

Due to its simplicity, we first show the asymptotic for P_z:

$$
\begin{aligned}
P_z &= \frac{\xi^2 + r^2 - r'^2}{\rho_1^2} \\
&= \frac{\xi^2}{\rho_1^2} - \frac{r'^2 - r^2}{\rho_1^2} \\
&= \frac{\xi^2}{\rho_1^2} - \frac{\sum_{k=1}^{\infty} \frac{(r^2)^{(k)}}{k!} \Delta\alpha^k}{(\sum_{k=1}^{\infty} \frac{z^{(k)}}{k!} \Delta\alpha^k)^2 + (\sum_{k=1}^{\infty} \frac{r^{(k)}}{k!} \Delta\alpha^k)^2} \\
&= \frac{\xi^2}{\rho_1^2} - \frac{1}{\Delta\alpha} \frac{\sum_{k=1}^{\infty} \frac{(r^2)^{(k)}}{k!} \Delta\alpha^{(k-1)}}{(\sum_{k=1}^{\infty} \frac{z^{(k)}}{k!} \Delta\alpha^{(k-1)})^2 + (\sum_{k=1}^{\infty} \frac{r^{(k)}}{k!} \Delta\alpha^{(k-1)})^2} \\
&= \frac{\xi^2}{\rho_1^2} - \frac{\sum_{k=2}^{\infty} \frac{(r^2)^{(k)}}{k!} \Delta\alpha^{(k-2)}}{(\sum_{k=1}^{\infty} \frac{z^{(k)}}{k!} \Delta\alpha^{(k-1)})^2 + (\sum_{k=1}^{\infty} \frac{r^{(k)}}{k!} \Delta\alpha^{(k-1)})^2} \\
&- \frac{1}{\Delta\alpha} \frac{2 r_\alpha r}{(\sum_{k=1}^{\infty} \frac{z^{(k)}}{k!} \Delta\alpha'^{(k-1)})^2 + (\sum_{k=1}^{\infty} \frac{r^{(k)}}{k!} \Delta\alpha^{(k-1)})^2} \\
&\approx \left(-\frac{2 r_\alpha r}{s_\alpha^2} \right) \frac{1}{\alpha' - \alpha} + \left(\frac{z_\alpha^2}{s_\alpha^2} - \frac{r_{\alpha\alpha} r + r_\alpha^2}{s_\alpha^2} \right) \qquad (\alpha' \approx \alpha) \\
&\Longrightarrow c_{P,z} = -\frac{2 r_\alpha r}{s_\alpha^2}, \qquad \text{(A.1)}
\end{aligned}
$$

where $\Delta\alpha = \alpha' - \alpha$ and, for example, $(r^2)^{(k)}$ is the k-th derivative of r^2 with respect to α' evaluated at $\alpha' = \alpha$. Similarly, we have

$$\begin{aligned} P_r &= \left(\frac{\xi}{\rho_1^2}\right)(\xi^2 + r^2 + r'^2) \\ &\approx \left(\frac{1}{\alpha' - \alpha}\frac{z_\alpha}{s_\alpha^2} + \frac{z_{\alpha\alpha}}{2s_\alpha^2}\right) \cdot \{2r^2 + 2r_\alpha r(\alpha' - \alpha)\} \qquad (\alpha' \approx \alpha) \\ &= \frac{1}{\alpha' - \alpha}\frac{2r^2 z_\alpha}{s_\alpha^2} + \left(\frac{r^2 z_{\alpha\alpha}}{s_\alpha^2} + \frac{2rr_\alpha z_\alpha}{s_\alpha^2}\right) + \mathcal{O}(|\alpha' - \alpha|) \\ &\Longrightarrow c_{P,r} = \frac{2r^2 z_\alpha}{s_\alpha^2}. \end{aligned} \tag{A.2}$$

for P_r, and

$$J \approx \begin{cases} \dfrac{1}{\alpha' - \alpha} - \dfrac{1}{2}\dfrac{\sin\alpha}{\cos\alpha} & \text{for } \alpha \in \left[0, \dfrac{\pi}{4}\right] \cup \left[\dfrac{3\pi}{4}, \pi\right] \\ \dfrac{1}{\alpha' - \alpha} + \dfrac{1}{2}\dfrac{\cos\alpha}{\sin\alpha} & \text{for } \alpha \in \left[\dfrac{\pi}{4}, \dfrac{3\pi}{4}\right] \end{cases} \qquad (\alpha' \approx \alpha) \tag{A.3}$$

for J.

Polynomial Expansions of Complete Elliptic Integrals

For $\lambda \approx 1$, we have

$$\begin{aligned} K(\lambda) &= \log 4 - \frac{1}{2}\log\zeta\left\{1 + \frac{\zeta}{4} + \frac{9}{64}\zeta^2 + ...\right\} \\ &\quad - \frac{1}{4}(1 - \log 4)\zeta + \frac{3}{128}(6\log 4 - 7)\zeta^2..., \end{aligned} \tag{A.4}$$

$$\begin{aligned} E(\lambda) &= 1 - \frac{\zeta\log\zeta}{4}\left\{1 + \frac{3}{8}\zeta + \frac{15}{64}\zeta^2 + ...\right\} \\ &\quad - \frac{\zeta}{4}\left\{-2\log 4 + 1 - \frac{24\log 2 - 13}{16}\zeta - \frac{3(5\log 2 - 3)}{16}\zeta^2 + ...\right\}, \end{aligned} \tag{A.5}$$

where $\zeta = 1 - \lambda^2$ [27].

Appendix B

Gram-Schmidt Process

Given a linearly independent collection of m square-integrable functions $\{\varphi_i\}_{1\le i\le m}$ on an interval I, the Gram-Schmidt process generates an orthonormal basis $\{u_i\}_{1\le i\le m}$ of the vector space spanned by the original system. The main objective here is to represent $\{u_i\}$ in terms of $\{\varphi_i\}$ as $u_i = \sum_{j=1}^{m} c_{i,j}\varphi_j$. In this algorithm, the first element u_1 is obtained by normalizing φ_1 as

$$u_1 = \varphi_1/\|\varphi_1\|_2, \quad \|f\|_2 = \left(\int_I f(x)^2 dx\right)^{\frac{1}{2}}, \tag{B.1}$$

and then the (unnormalized) i–th element $\tilde{u}_i$ $(2 \le i \le m)$ is found by subtracting the components in the u_j directions for $1 \le j \le i-1$:

$$\begin{aligned}
\tilde{u}_i &= \varphi_i - \sum_{j=1}^{i-1} < \varphi_i, u_j > u_j \\
&= \varphi_i - \sum_{j=1}^{i-1} \left(< \varphi_i, \sum_{l=1}^{j} c_{j,l}\varphi_l > \sum_{k=1}^{j} c_{j,k}\varphi_k \right) \\
&= \varphi_i - \sum_{j=1}^{i-1} \left(\sum_{l=1}^{j} c_{j,l} < \varphi_i, \varphi_l > \right) \left(\sum_{k=1}^{j} c_{j,k}\varphi_k \right) \\
&= \varphi_i - \sum_{j=1}^{i-1} \left(\sum_{k=1}^{j} \left(\sum_{l=1}^{j} c_{j,l} < \varphi_i, \varphi_l > \right) c_{j,k}\varphi_k \right) \\
&= \sum_{j=1}^{i} \tilde{c}_{i,j}\varphi_j.
\end{aligned} \tag{B.2}$$

To normalize $\tilde{u}_i$, its L^2 norm is computed using the coefficients $\{\tilde{c}_{i,j}\}_{1\le j\le i}$:

$$\begin{aligned}\|\tilde{u}_i\|_2^2 &=< \sum_{j=1}^{i} \tilde{c}_{i,j}\varphi_j, \sum_{k=1}^{i} \tilde{c}_{i,k}\varphi_k > \\ &= \sum_{j=1}^{i} \tilde{c}_{i,j} < \varphi_j, \sum_{k=1}^{i} \tilde{c}_{i,k}\varphi_k > \\ &= \sum_{j=1}^{i} \tilde{c}_{i,j}\left(\sum_{k=1}^{i} \tilde{c}_{i,k} < \varphi_j, \varphi_k >\right), \end{aligned} \tag{B.3}$$

and the normalized coefficients $\{c_{i,j}\}_{1\le j\le i}$, where $c_{i,j} = \tilde{c}_{i,j}/\|\tilde{u}_i\|_2$, are stored for representing u_i. Also, the accuracy of the orthonormalization process can be estimated by performing the following matrix operation:

$$\begin{aligned}< u_i, u_j > &=< \sum_{k=1}^{i} c_{i,k}\varphi_k, \sum_{l=1}^{j} c_{j,l}\varphi_l > \\ &= \sum_{k=1}^{i} c_{i,k}\left(\sum_{l=1}^{j} c_{j,l} < \varphi_k, \varphi_l >\right). \end{aligned} \tag{B.4}$$

If the result is the identity matrix up to a given tolerance, the Gram-Schmidt process has been successfully completed. Otherwise, additional digits in the floating-point arithmetics are required for further improvements.

Bibliography

[1] J. Eggers. Nonlinear dynamics and breakup of free-surface flows. *Rev. Mod. Phys.*, 69:865, 1997.

[2] T.Y. Hou, J.S. Lowengrub, and M.J. Shelley. The long-time motion of vortex sheets with surface tension. *Phys. Fluids*, 9:1933–1954, 1997.

[3] D. Leppinen and J.R. Lister. Capillary pinch-off in inviscid fluids. *Phys. Fluids*, 15:568–578, 2003.

[4] M. Nitsche and P.H. Steen. Numerical simulations of inviscid capillary pinchoff. *J. Comput. Phys.*, 200:299–324, 2004.

[5] J.C. Burton and P. Taborek. Two-dimensional inviscid pinch-off: An example of self-similarity of the second kind. *Phys. Fluids*, 19:102109, 2007.

[6] G.R. Baker, D.I. Meiron, and S.A. Orszag. Generalized vortex methods for free-surface flow problems. *J. Fluid Mech.*, 123:477–501, 1982.

[7] A.H. Barnett, J. Magland, and L. af Klinteberg. A parallel nonuniform fast Fourier transform library based on an "exponential of semicircle" kernel. *SIAM J. Sci. Comput.*, 41(5):C497–C504, 2019.

[8] Q. Nie. The nonlinear evolution of vortex sheets with surface tension in axisymmetric flows. *J. Comput. Phys.*, 174:438–459, 2001.

[9] C.L. Epstein and M. Gage. The curve shortening flow. In A.J. Chorin and A.J. Majda, editors, *Wave Motion: Theory, Modelling, and Computation*, Math. Sci. Res. Inst. Publ., pages 15–59. Springer, New York, 1987.

[10] J. Ma, V. Rokhlin, and S. Wandzura. Gaussian quadrature rules for systems of arbitrary functions. *SIAM J. Numer. Anal.*, 33(3):971–996, 1996.

[11] H. Takahasi and M. Mori. Double exponential formulas for numerical integration. *Publ. RIMS Kyoto Univ.*, 9:721–741, 1974.

[12] K. Koga. Signal processing approach to mesh refinement in simulations of axisymmetric droplet dynamics. *J. Comput. Appl. Math.*, 383:113131, 2021.

[13] K. Koga and J. Wilkening. A new discretization of axisymmetric vortex sheets with surface tension. in preparation.

[14] R.E. Caflisch and X. Li. Lagrangian theory for 3D vortex sheets with axial or helical symmetry. *Transport Theory Statist. Phys.*, 21:559–578, 1992.

[15] D.W. Moore. The spontaneous appearance of a singularity in the shape of an evolving vortex sheet. *Proc. R. Soc. Lond. A.*, 365:105–119, 1979.

[16] T.Y. Hou, J.S. Lowengrub, and M.J. Shelley. Removing the stiffness from interfacial flows with surface tension. *J. Comput. Phys.*, 114:312–338, 1994.

[17] R. Krasny. A study of singularity formation in a vortex sheet by the point-vortex approximation. *J. Fluid Mech.*, 167:65–93, 1986.

[18] N.D. Robinson and P.H. Steen. Observations of singularity formation during the capillary collapse and bubble pinch-off of a soap film bridge. *J. Colloid and Interface Science*, 241:448–458, 2001.

[19] G.K. Batchelor. *An Introduction to Fluid Mechanics*. Cambridge University Press, Cambridge, 1967.

[20] J.C. Burton and P. Taborek. Role of dimensionality and axisymmetry in fluid pinch-off and coalescence. *Phys. Rev. Lett.*, 98:224502, 2007.

[21] D. Gabor. Theory of communication. *J. Inst. Elect. Engrs. (Pt. III)*, 93:429–441, 1946.

[22] C. Muscalu and W. Schlag. *Classical and Multilinear Harmonic Analysis, Volume 1*. Cambridge University Press, Cambridge, 2013.

[23] S.O. Rice. Envelopes of narrow-band signals. *Proc. IEEE*, 70(7):692–699, 1982.

[24] L. Cohen. *Time-Frequency Analysis: Theory and Applications*. Prentice Hall, Upper Saddle River, 1995.

[25] C. Bauer, R. Freeman, T. Frenkiel, J. Keeler, and A.J. Shaka. Gaussian pulses. *J. Magn. Reson.*, 58:442–457, 1984.

[26] M. Nitsche. Axisymmetric vortex sheet motion: accurate evaluation of the principal value integral. *SIAM J. Sci. Comput.*, 21(3):1066–1084, 1999.

[27] P.F. Bryd and M.D. Friedman. *Handbook of Elliptic Integrals for Engineers and Physicists*. Springer-Verlag, Berlin/New York, 1953.

[28] B. de Bernardinis and D.W. Moore. A ring-vortex representation of an axi-symmetric vortex sheet. In M.Y. Hussaini and M.D. Salas, editors, *Studies of Vortex Dominated Flows*, pages 33–43. Springer-Verlag, Berlin/New York, 1987.

[29] Q. Nie and G. Baker. Application of adaptive quadrature to axi-symmetric vortex sheet motion. *J. Comput. Phys.*, 143:49–69, 1998.

[30] A.S. Kronrod. *Nodes and Weights of Quadrature Formulas*. Consultants Bureau, New York, 1965.

[31] R. Piessens and M. Branders. The evaluation and application of some modified moments. *BIT Numer. Math.*, 13:443–450, 1973.

[32] A. Sidi and M. Israeli. Quadrature methods for periodic singular and weakly singular fredholm integral equations. *J. Sci. Comput.*, 3:201–231, 1988.

[33] M. Nitsche, H.D. Ceniceros, A.L. Karniala, and S. Naderi. High order quadratures for the evaluation of interfacial velocities in axi-symmetric Stokes flows. *J. Comput. Phys.*, 229:6318–6342, 2010.

[34] B.K. Alpert. Hybrid Gauss-trapezoidal quadrature rules. *SIAM J. Sci. Comput.*, 20(5):1551–1584, 1999.

[35] S.J. Karlin and W.J. Studden. *Tchebycheff Systems: With Applications in Analysis and Statistics*. John Wiley (Interscience), New York, 1966.

[36] L.N. Trefethen. Is Gauss quadrature better than Clenshaw-Curtis? *SIAM Review*, 50(1):67–87, 2008.

[37] L.N. Trefethen and J.A.C. Weideman. The exponentially convergent trapezoidal rule. *SIAM Review*, 56(3):385–458, 2014.

[38] B. Adcock, J. Martin-Vaquero, and M. Richardson. Resolution-optimal exponential and double-exponential transform methods for functions with endpoint singularities. *SIAM J. Sci. Comput.*, 39(1):A164–A187, 2017.

[39] J. Nocedal and S.J. Wright. *Numerical Optimization*. Springer, New York, 2006.

[40] J. Bremer, Z. Gimbutas, and V. Rokhlin. A nonlinear optimization procedure for generalized Gaussian quadratures. *SIAM J. Sci. Comput.*, 32(4):1761–1788, 2010.

[41] J.E. Dennis, Jr. and R.B. Schnabel. *Numerical Methods for Unconstrained Optimization and Nonlinear Equations*. Prentice-Hall, Englewood Cliffs, NJ, 1983.

[42] M. Abramowitz and I.A. Stegun. *Handbook of Mathematical Functions*. Dover Publications, New York, 1965.

[43] J. Cheng, M. Grossman, and T. McKercher. *Professional CUDA C Programming*. John Wiley & Sons, Inc., New York, 2014.

[44] L. Greengard and J. Lee. Accelerating the nonuniform fast Fourier transform. *SIAM Review*, 46(3):443–454, 2004.

[45] J. Keiner, S. Kunis, and D. Potts. Using NFFT 3—a software library for various nonequispaced fast Fourier transforms. *ACM Trans. Math. Software*, 36(4):19, 2009.

[46] R. Almgren. Singularity formation in Hele–Shaw bubbles. *Phys. Fluids*, 8:344–352, 1996.

[47] G.R. Baker and M.J. Shelley. On the connection between thin vortex layers and vortex sheets. *J. Fluid Mech.*, 215:161–194, 1990.

[48] K. Mikula and D. Ševčovič. Computational and qualitative aspects of evolution of curves driven by curvature and external force. *Comput. Vis. Sci,*, 6:211–225, 2004.

[49] H. Lamb. *Hydrodynamics*. Cambridge University Press, Cambridge, 1932.

[50] J.W.S. Rayleigh. On the capillary phenomena of jets. *Proc. R. Soc. Lond.*, 29:71–97, 1879.

[51] J. Eggers, M.A. Fontelos, D. Leppinen, and J.H. Snoeijer. Theory of the collapsing axisymmetric cavity. *Phys. Rev. Lett.*, 98:094502, 2007.

[52] A. Deblais, M.A. Herrada, I. Hauner, K.P. Velikov, T. van Roon, H. Kellay, J. Eggers, and D. Bonn. Viscous effects on inertial drop formation. *Phys. Rev. Lett.*, 121:254501, 2018.

[53] D.M. Ambrose. Singularity formation in a model for the vortex sheet with surface tension. *Math. Comput. Simul.*, 80:102–111, 2009.

[54] T.S. Lundgren and N.N. Mansour. Oscillations of drops in zero gravity with weak viscous effects. *J. Fluid Mech.*, 194:479–510, 1988.

[55] D.M. Ambrose and J. Wilkening. Computation of symmetric, time-periodic solutions of the vortex sheet with surface tension. *Proc. Natl. Acad. Sci.*, 107/8:3361–3366, 2010.

List of publications

K. Koga, Signal processing approach to mesh refinement in simulations of axisymmetric droplet dynamics, *J. Comput. Appl. Math.*, **383**, 113131, 2021.
DOI Link: https://doi.org/10.1016/j.cam.2020.113131

K. Koga and J. Wilkening, A new discretization of axisymmetric vortex sheets with surface tension, in preparation.

(Due to the Article Sharing policy of the journal, the DOI link of the published journal article embedded in the thesis is shown to indicate the copyright information.)

Other publications

K. Koga and M. Funakoshi, Recent Progress in Simulations of 3D Vortex Sheets with Surface Tension, In *Mathematical Insights into Advanced Computer Graphics Techniques*, pp. 119--129, Springer Singapore, 2019.